Biomechanics and Modeling in Mechanobiology _####################_
https://doi.org/10.1007/s10237-026-02065-7

ORIGINAL PAPER

Computational hemodynamic analysis of renal blood flow and the impact of outflow boundary conditions

Fenfen Qi[1] · Yingzhi Liu[1] · Rongliang Chen[2] · Xiao-Chuan Cai[1]

Received: 27 September 2025 / Accepted: 17 March 2026

Abstract

Hemodynamic analysis is an essential tool for predicting the behavior of blood flows and assessing the risk of renovascular diseases. In this paper, by employing a CFD-based finite element method coupled with an efficient parallel algorithm for the unsteady incompressible Navier–Stokes equations, we conduct a comprehensive investigation of renal hemodynamics and the impact of outflow boundary conditions in patient-specific models of normal, stenotic, and aneurysmal arteries featuring rich small-branch networks. Based on the hemodynamic analysis for the severe stenosis (area stenosis $>$ 87%) and the aneurysm (diameter $=$ 13.3 mm), we observe a pressure drop exceeding 10 mmHg and a distal-to-proximal pressure ratio below 0.9 for these lesions, which is considered hemodynamically significant and likely induces renovascular hypertension. Furthermore, we reveal that the low wall shear stress and complex vortices with bidirectional flow occur on the inner wall downstream of this stenosis, which play a critical role in driving atherosclerotic plaque formation. Through virtual aneurysm reconstruction and numerical simulation, we demonstrate that the presence of a renal aneurysm alters local flow patterns and pressure distributions. Numerical results for both healthy and pathological renal arteries show that outflow boundary conditions have a significant impact on the global distribution of pressure and local flow patterns near the outlets. Compared with constant pressure and resistance outflow boundary conditions, the two-element Windkessel model, through adjustments of its resistance and capacitance parameters, can provide more physiological flow and pressure distributions, particularly in capturing realistic pulsatile waveforms, pressure ranges, and distal flow patterns. Moreover, a sensitivity analysis of the resistance in the Windkessel boundary condition shows a negligible impact on the pressure drop and only a minor effect on the renal fractional flow reserve (a change of less than 3% for a 20% variation in resistance). When focusing solely on the hemodynamics within stenotic and aneurysmal lesions located far from the outlets, both the constant pressure and Windkessel boundary conditions yield comparable results for key lesion-specific hemodynamic indicators, including renal fractional flow reserve and pressure drop in the stenosis, and wall shear stress and oscillatory shear index in the aneurysm.

Keywords Renal blood flows · Computational fluid dynamics · Renal fractional flow reserve · Outflow boundary conditions · Renovascular diseases · Hypertension

1 Introduction

Of all the organs in the human body, the kidneys are vital components in maintaining metabolic balance through waste filtration and reabsorption of essential electrolytes and water. The critical physiological process relies on the robust vascular supply, with the renal artery branching from the abdominal aorta to deliver approximately 19% of cardiac output, ensuring adequate kidney perfusion (Valentin 2002). However, kidney function can be damaged by severe renovascular dis-

✉ Xiao-Chuan Cai
xccai@um.edu.mo

Fenfen Qi
yc27956@um.edu.mo

Yingzhi Liu
yingzhiliu@um.edu.mo

Rongliang Chen
rl.chen@siat.ac.cn

[1] Department of Mathematics, University of Macau, Macau, People's Republic of China

[2] Shenzhen Institutes of Advanced Technology, Chinese Academy of Sciences, Shenzhen, People's Republic of China

eases, including renal artery stenosis (RAS) and renal artery aneurysm (RAA). RAS, particularly the atherosclerotic RAS, is clinically significant due to its strong association with systemic hypertension (Andayesh et al. 2020) and multiple syndromes such as secondary hypertension (Down et al. 2013) and ischemic nephropathy (Weber and Dieter 2014), leading to irreversible kidney damage and driving the progression of chronic kidney disease (CKD) (Dobrek 2021). In contrast to intracranial aneurysms, where rupture risk is a primary concern, RAAs are rare (0.1%), slow-growing (0.086 ± 0.08cm/year), and rarely rupture (0.3%) even above 2cm (Klausner et al. 2015). However, they are strongly linked to renovascular hypertension (Coleman and Stanley 2015; Klausner et al. 2015). This association is most likely induced by altered hemodynamics that create a functional RAS (Steuer et al. 2019; Dobrek 2021). Therefore, accurate assessment of these renovascular diseases is needed for the proper diagnosis, treatment and follow-up prognosis. Hemodynamics serves as a fundamental methodology for analyzing and assessing renal vascular function. Numerical techniques are useful non-invasive tools that are widely applied in hemodynamic simulations for aortic (Pirola et al. 2017; Boccadifuoco et al. 2018), abdominal (Qin et al. 2021), cerebral (Saalfeld et al. 2019; Chen et al. 2020), carotid (Xu et al. 2018), and coronary arteries (Yan et al. 2022; Di Gregorio et al. 2021). In contrast, research on renal artery hemodynamic simulation remains very limited (Andayesh et al. 2020; Down et al. 2013; Qi et al. 2025a, b) and requires further development.

Various blood flow models for numerical hemodynamic simulations have been developed, which are broadly divided into two categories: low-dimensional models (Zhou et al. 2019; Steele 2007) (including 0D, 1D, and tube-load models) and high-dimensional models (Grinberg et al. 2009; Quarteroni et al. 2016) (such as 2D and 3D models). Low-dimensional approaches with low computational costs can efficiently describe the average hemodynamic properties without concerning individual anatomical variations such as specific stenosis severity and aneurysm morphology (Zhou et al. 2019; Xiao et al. 2014). To perform high-fidelity hemodynamic simulation and comprehensive analysis in regions of vascular pathology, offering valuable insights for risk assessments associated with various vascular conditions (Meng et al. 2014; Byrne et al. 2014), it is essential to employ full 3D or multiscale (Formaggia et al. 1999, 2001) blood flow models. In 3D blood flow models, the unsteady incompressible Navier–Stokes equations are widely adopted as the governing equations. In blood rheology, blood viscosity is often assumed to be constant (Newtonian) for flows in large arteries with a diameter greater than approximately 0.5mm (Taylor and Yamaguchi 1994; Perktold et al. 1991). Even for arterial pathologies like aneurysms and stenosis, the Newtonian model remains reliable for hemodynamic calculations unless significantly low-shear-rate regions are identified (Morales et al. 2013; Arzani 2018; Liu et al. 2021). In contrast, non-Newtonian behavior becomes more critical for blood flow in small arteries with a diameter below about 3.5μm (Brujan 2010). Many studies of the renal hemodynamics (Mandaltsi et al. 2018; Berg et al. 2019) limit their computational domain to the main renal artery, omitting its branches. This is primarily because segmenting the renal vasculature from medical images remains a considerable challenge, owing to its complex anatomical structure, interference from surrounding soft tissues, and low contrast in conventional imaging modalities. From the viewpoint of fluid mechanics, the vascular structure significantly shapes blood flow characteristics, especially in investigations of microcirculation (Lipowsky 2005) and renal vasculature (Deng and Tsubota 2022). In practice, the fine-scale representation of the distal vasculature is particularly critical for renal vascular modeling, which ensures a high-fidelity hemodynamic result for accurately assessing the risk of renovascular diseases with different severity and anatomical depths of lesions. Moreover, the detailed outflow rate distribution directly reflects renal perfusion dynamics, which can be used to evaluate local renal physiological function and pathological changes (Klepaczko et al. 2018). Our study constructs a comprehensive computational domain from high-resolution medical images, including the major renal arteries along with a rich vasculature of small branches, with diameters down to approximately 1 mm. The Newtonian fluid model is reliable for vessels at this scale. Therefore, it is adopted in this work to simulate the renal blood flow. However, clinical medical imaging techniques are inherently limited by spatial resolution, making it challenging to further reconstruct the distal vascular network.

To address this limitation, a common practice is to couple the 3D unsteady incompressible Navier–Stokes equations with appropriate boundary conditions (BCs) for enhancing the physiological accuracy of renal vascular models. The distal/outflow BCs, which provide a low-dimensional approximation of the blood flow behavior in downstream vascular networks, significantly affect the accuracy of numerical simulations. The simple outflow BC is the constant pressure BC (Deng and Tsubota 2022) that prescribes a uniform pressure at all renal arterial outlets. While straightforward to implement, it lacks the realism needed for physiological accuracy. To account for the resistance of the downstream arteries and arterioles, the implicit resistance BC was developed (Mandaltsi et al. 2018) by employing a linear relationship between the pressure and the flow rate at each outlet. In contrast to the constant pressure BC, this BC is more complex and computationally demanding because of its implicit dependence on velocity. The 0D Windkessel models are widely used to simulate blood flow in downstream vascular networks by an electric circuit analog, using lumped parameters of resistance (representing flow resistance) and capacitance (representing

wall compliance). The two-element RC Windkessel (RC) model consists of a resistance in parallel with a capacitance (Westerhof et al. 2009). The three-element RCR Windkessel (RCR) model introduces a proximal characteristic resistance in series with a parallel combination of a capacitance and a distal resistance from the arterioles and capillaries (Vignon-Clementel et al. 2006; Formaggia et al. 2006; Les et al. 2010). Compared with the resistance and RC BCs, the RCR BC offers a more complete hemodynamic representation, capturing both the pulsatile and resistive behavior of the arterial system. To avoid high-frequency oscillations in the RCR BC, a relatively small characteristic resistance is typically required, which means a BC similar to the RC BC (Grinberg and Karniadakis 2008). Applications of these outflow BCs to hemodynamic simulations in cardiovascular, aortic and cerebral arterial systems can be found in Grinberg and Karniadakis (2008); Pirola et al. (2017); Boccadifuoco et al. (2018); Madhavan and Kemmerling (2018); Saalfeld et al. (2019); Xu et al. (2018). Considering the special functions of the kidney, renal vascular structure and common sites of renovascular lesions, it is necessary to systematically investigate how outflow BCs influence the behavior of renal blood flow in lesions and the outflow rate distribution to identify a suitable BC for advancing our understanding of renal hemodynamics and related disease mechanisms.

The computational effort of solving three-dimensional blood flow problems is always challenging and requires efficient discretized methods and robust solvers to address complex geometries and nonlinear properties of blood flows. For the renal blood flow simulation, we employ a stabilized finite element method (Franca and Frey 1992) and the second-order backward differentiation formula for the spatial and temporal discretizations, respectively. Following the discretization of the governing equations, the Newton-Krylov method is used for the large-scale, sparse and nonlinear systems, leveraging the quadratic convergence of the Newton method when the initial guess is near the solution and the robustness of Krylov subspace methods. In the Newton-Krylov framework, the Newton method serves as the outer iterative scheme, iteratively updating approximate solutions along Newton directions, while the Krylov subspace method acts as the inner iterative scheme, approximating Newton directions from the Krylov subspaces of the Jacobian system. Considering the complexity of the Jacobian system due to the incompressibility condition, we use a robust two-level additive Schwarz preconditioner, with a one-dimensional central-line coarse preconditioner (Liu et al. 2023a, b), which was first introduced using a reduced 1D blood flow model (Formaggia et al. 1999) defined along the centerline of arteries (Liu and Cai 2021).

This study aims to provide a comprehensive CFD-based analysis of renal hemodynamics by employing patient-specific models of normal, stenotic, and aneurysmal arteries with rich branching networks. By analyzing the complex flow patterns in stenotic and aneurysmal lesions, we assess their hemodynamic risk status and provide insights into their association with hypertension, which is frequently observed in the natural history of these renovascular diseases (Subramanian et al. 2005; Coleman and Stanley 2015; Zhang et al. 2023). Furthermore, we investigate the impact of outflow BCs (constant pressure, resistance, and RC Windkessel) on hemodynamic parameters: the global pressure distribution, flow patterns, distal flow rate, and critical risk indicators, especially the renal fractional flow reserve (rFFR) (Subramanian et al. 2005; White 2006), pressure drop (PD) (Yim et al. 2004; Andayesh et al. 2020; Subramanian et al. 2005), wall shear stress (WSS), and oscillatory shear index (OSI), within the region of renal artery lesion. The rest of this paper is organized as follows. In Section 2, we detail the geometric reconstruction of patient-specific renal arteries from CT imaging, describe the computational mathematical model with three outflow BCs and a stabilized finite element discretization, and then introduce an efficient and scalable parallel algorithm to solve the large-scale and sparse nonlinear system. In Section 3, some numerical experiments for normal and abnormal renal arteries are presented to analyze the hemodynamics and evaluate the influence of outflow BCs. Finally, we summarize the conclusions in Section 4.

2 Methodology

2.1 Image segmentation and geometric reconstruction

In Fig. 1, we show three patient-specific renal arterial geometries: the stenotic one, the normal one and the aneurysmal one, each featuring one inlet and 10, 19, and 14 outlet branches, respectively. These geometries are reconstructed from CT images with suitable threshold and region-growing methods in Mimics. For a more accurate simulation of the blood flow, some postprocessing techniques such as smoothing, are applied to refine and regularize the geometries. In the stenotic case, where the stenosis is located near the renal artery inlet, we extend the inlet with a 10 mm straight segment to facilitate the development of a fully developed flow profile. This extension is crucial for accurately evaluating the effect of the stenosis on flow behavior and understanding the complex hemodynamics in stenotic regions. For the aneurysm case, we consider a bilateral renal artery geometry, where the abdominal aorta is truncated for the prescription of the inlet boundary and the large abdominal aorta outlet boundary.

2.2 Mathematical model

To model the blood flow in a renal arterial domain $\Omega \in \mathbb{R}^3$ over a cardiac cycle T, we consider the unsteady incompressible Navier–Stokes equations

$$\begin{cases} \rho\left(\dfrac{\partial \boldsymbol{u}}{\partial t} + \boldsymbol{u}\cdot\nabla\boldsymbol{u}\right) - \mu\Delta\boldsymbol{u} + \nabla p = \boldsymbol{0}, & \text{in } \Omega\times(0,T), \\ \nabla\cdot\boldsymbol{u} = 0, & \text{in } \Omega\times(0,T), \\ \boldsymbol{u}(\boldsymbol{x},0) = \boldsymbol{u}_0(\boldsymbol{x}), & \text{in } \Omega, \end{cases} \tag{1}$$

where ρ and μ are the blood density and the viscosity, $\boldsymbol{u}_0$ is the initial velocity, $\boldsymbol{u}$ and p are the velocity and the pressure. The governing equation (1) characterizes the conservation of momentum and mass for blood flow within the arterial domain of interest. Denote by $\partial\Omega = \Gamma_I \cup \Gamma_W \cup \Gamma_O$ the boundary of the domain, where Γ_I, Γ_W and $\Gamma_O = \bigcup_{i=1}^{m} \Gamma_O^i$ are the inlet cross section, the arterial wall and the m outlet cross sections, respectively. On the inlet and wall, we impose a velocity Dirichlet BC and a no-slip BC, as follows,

$$\begin{aligned} &\boldsymbol{u} = \boldsymbol{u}_I(t), && \text{on } \Gamma_I\times(0,T), \\ &\boldsymbol{u} = \boldsymbol{0}, && \text{on } \Gamma_W\times(0,T), \end{aligned} \tag{2}$$

where $\boldsymbol{u}_I(t)$ is a given time-dependent pulsatile waveform from (Taylor et al. 1998) with a parabolic velocity profile, shown in the left subfigure of Fig. 2. On the outlets, we consider a general pressure BC,

$$p = g(\boldsymbol{u}, t), \quad \text{on } \Gamma_O\times(0,T), \tag{3}$$

here $g(\boldsymbol{u}, t)$ is a function that may depend on $\boldsymbol{u}$ and t.

2.3 Three outflow boundary conditions

Considering the challenges in measuring outlet velocity data, the outlet pressure BC (3) is implemented to approximate the pressure at the outlets. To investigate the impact of the pressure BC (3) on numerical results, we focus on three types of outflow BCs used in the simulation of blood flow: (1) the constant pressure BC; (2) the resistance BC; (3) the RC Windkessel BC.

We first consider the simple constant pressure BC (Vignon-Clementel et al. 2006)

$$p = p_c, \quad \text{on } \Gamma_O\times(0,T), \tag{4}$$

where p_c is a given constant pressure for all renal arterial outlets. The condition is suitable for sufficiently small distal arterial outlets, as the pressure at these outlets remains nearly constant. However, in the implementation, the diameters of

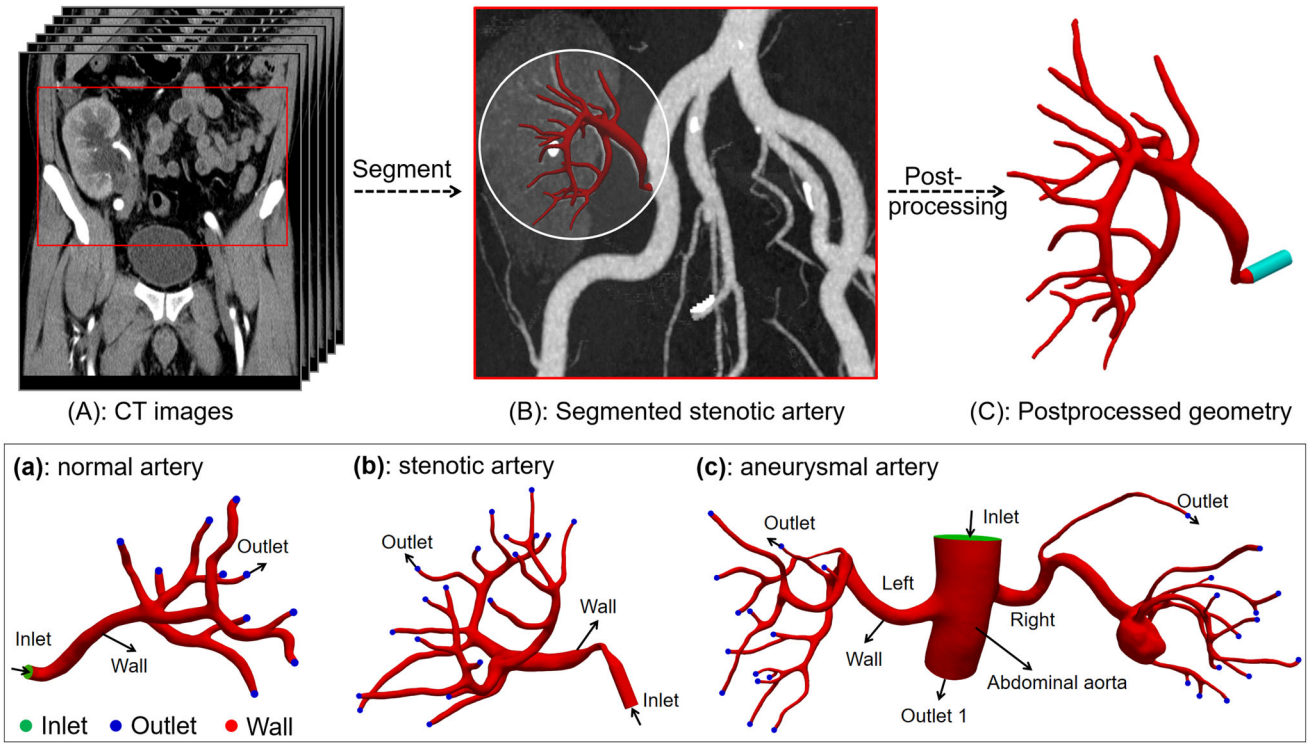

Fig. 1 Three patient-specific renal arterial geometries reconstructed from CT images, including the normal, the stenotic (with an inlet extension in light blue), and the aneurysmal cases, with the inlet, outlets and wall highlighted in green, blue, and red, respectively

outlets of the computational artery are limited by the resolution of CT images, and the constant pressure BC neglects the effects of downstream small arteries on blood flow.

The resistance BC (Vignon-Clementel et al. 2006) is based on the assumption of a linear dependence between the pressure and the blood flux

$$p = R_r^i Q_i, \quad \text{on } \Gamma_O^i \times (0,T), \quad i = 1,2,\cdots,m, \tag{5}$$

where $Q_i(t) = \int_{\Gamma_O^i} \boldsymbol{u}(t)\cdot\boldsymbol{n}\mathrm{d}\Gamma_O^i$ is the blood flux at the ith outlet with the outward unit normal vector $\boldsymbol{n}$ and R_r^i is a constant resistance. By prescribing a suitable resistance R_r^i at each outlet, the BC (5) can account for their influence on the pressure. Analogous to the Murray's law (Lan et al. 2018), these outlet resistances can be determined by a total resistance R_r and the outlet areas $\{S_i\}_{i=1}^m$, as given by

$$R_r^i = R_r S_i^{-\frac{3}{2}} \left(\sum_{i=1}^m S_i^{\frac{3}{2}}\right), \quad i = 1,2,\cdots,m. \tag{6}$$

Compared with the explicit constant pressure BC, the resistance BC implicitly reflects the relationship between the pressure and the flux at each outlet through the integral of the velocity, which increases both implementation and computational complexity.

The third type of the outflow BC is related to a RC Windkessel model (Westerhof et al. 2009)

$$C_w^i \frac{dp(t)}{dt} + \frac{p(t)}{R_w^i} = Q_i(t), \quad \text{on } \Gamma_O^i \times (0,T), \quad i = 1,2,\cdots,m, \tag{7}$$

where R_w^i and C_w^i are the constant resistance and capacitance, respectively. The Windkessel model (7), formulated as an ordinary differential equation, is analogous to an electric-circuit model, as illustrated in Fig. 2 with $R_{w1}^i = 0$ and $R_{w2}^i = R_w^i$. It describes the influence of the resistance and capacitance at the downstream vasculature on the region of interest. The analytical solution of (7) with a zero distal pressure is given by

$$p(t) = p(0)e^{-\frac{t}{R_w^i C_w^i}} + \int_0^t \frac{e^{-(t-s)/R_w^i C_w^i}}{C_w^i} Q_i(s)ds, \tag{8}$$

which is implicitly relies on the velocity $\boldsymbol{u}$.

According to the principles for parallel circuits, Murray's law and the relationship between capacitances and outlet areas, the parameters $\{R_w^i\}_{i=1}^m$ and $\{C_w^i\}_{i=1}^m$ are determined using the following rules (Lan et al. 2018)

$$R_w^i = R_w S_i^{-\frac{3}{2}} \left(\sum_{i=1}^m S_i^{\frac{3}{2}}\right), \quad C_w^i = C_w S_i \left(\sum_{i=1}^m S_i\right)^{-1}, \tag{9}$$

where R_w and C_w are the total resistance and capacitance, respectively. Note that the resistance BC is a special case of the Windkessel BC without the capacitances, i.e., $C_w^i = 0, i = 1,\ldots,m$. Compared with the resistance BC, the Windkessel BC considers the elasticity of downstream small arterial networks, resulting in a more complex relationship between the pressure and the flux.

Remark 1 The implicit relationship between the pressure and flux from the resistance and RC Windkessel BCs can preserve a physiological periodic phenomenon. We assume that Q_i is periodic with period T. The property is trivial for the resistance BC (5) at any time t

$$p(t+T) - p(t) = R_r^i(Q_i(t+T) - Q_i(t)) = 0.$$

For the RC Windkessel BC, from the analytical solution (8), we have

$$\begin{aligned} p(t+T) - p(t) =& p(0)e^{-\frac{t}{R_w^i C_w^i}}\left(e^{-\frac{T}{R_w^i C_w^i}} - 1\right) \\ &+ \int_0^{t+T} \frac{e^{-(t+T-s)/R_w^i C_w^i}}{C_w^i} Q_i(s)ds \\ &- \int_0^t \frac{e^{-(t-s)/R_w^i C_w^i}}{C_w^i} Q_i(s)ds \\ =& p(0)e^{-\frac{t}{R_w^i C_w^i}}\left(e^{-\frac{T}{R_w^i C_w^i}} - 1\right) \\ &+ \int_{-T}^0 \frac{e^{-(t-s)/R_w^i C_w^i}}{C_w^i} Q_i(s)ds \\ =& p(0)e^{-\frac{t}{R_w^i C_w^i}}\left(e^{-\frac{T}{R_w^i C_w^i}} - 1\right) \\ &+ \int_0^T \frac{e^{-(t+T-s)/R_w^i C_w^i}}{C_w^i} Q_i(s)ds, \end{aligned} \tag{10}$$

which indicates that the difference $p(t+T) - p(t)$ decays exponentially to zero with respect to t and therefore implies the periodicity after several cardiac cycles, as illustrated in Fig. 3.

Remark 2 In Windkessel models, two-element RC and three-element RCR Windkessel models are widely used. In this paper, we adopt the RC model based on the following considerations that it involves a single resistance parameter, can filter high-frequency oscillations (Grinberg and Karniadakis 2008) from the flowrate Q_i, and is an effective approximation of the RCR model for realistic small values of R_{w1}^i. In

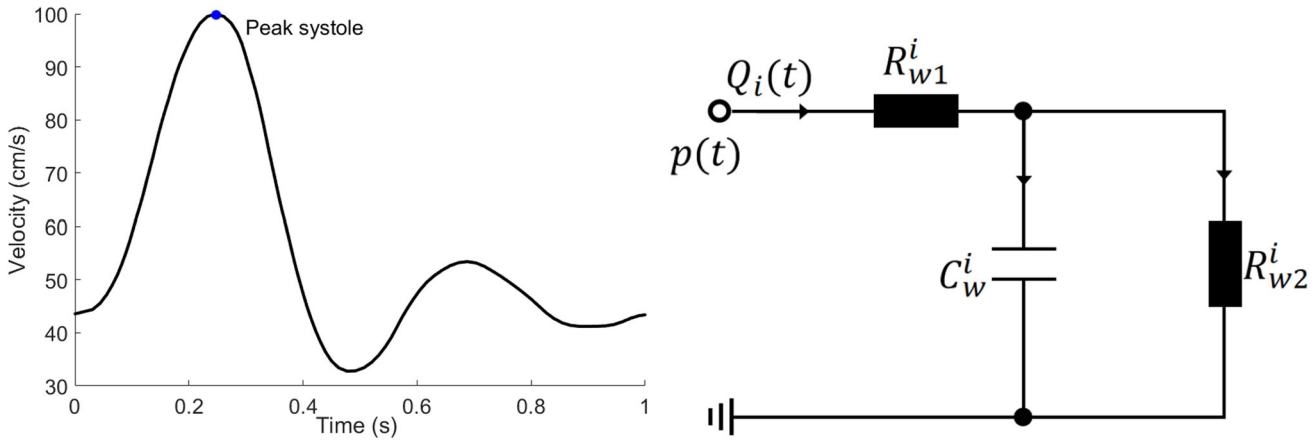

Fig. 2 Pulsatile inflow velocity profile over one cardiac cycle (left) and the circuit diagram of the RC ($R^i_{w1} = 0$, $R^i_{w2} = R^i_w$) and RCR Windkessel models (right)

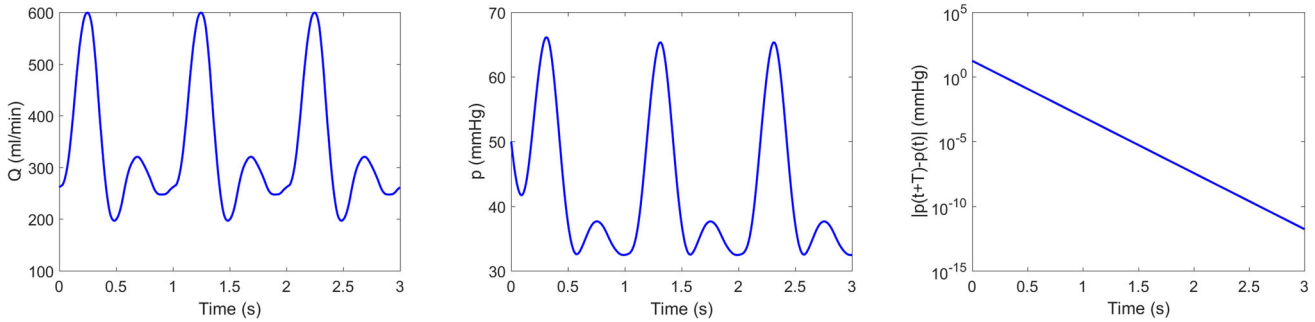

Fig. 3 Periodic phenomenon observed in the RC Windkessel model, where $R_w = 10^4$, $C_w = 10^{-5}$, $p(0) = 50$mmHg. From left to right: (1) A given periodic flowrate Q with period $T = 1$s; (2) The analytical RC pressure based on the given Q; (3) The pressure difference function $|p(t+T) - p(t)|$ with respect to t

fact, the RCR Windkessel model on Γ^i_O, $i = 1, 2, \cdots, m$, as shown in Fig. 2, is given by

$$C^i_w \frac{dp(t)}{dt} + \frac{p(t)}{R^i_{w2}} = C^i_w R^i_{w1} \frac{dQ_i(t)}{dt} + \frac{(R^i_{w1} + R^i_{w2})Q_i(t)}{R^i_{w2}}, \tag{11}$$

where R^i_{w1} and R^i_{w2} are proximal characteristic and distal resistances, respectively, which implies the following analytical solution

$$p(t) = \left(p(0) - R^i_{w1} Q_i(0)\right) e^{-\frac{t}{R^i_{w2} C^i_w}} + R^i_{w1} Q_i(t) + \int_0^t \frac{e^{-(t-s)/R^i_{w2} C^i_w}}{C^i_w} Q_i(s) ds. \tag{12}$$

To observe the impact of high-frequency oscillations of Q_i on the pressure of RC and RCR models, we adopt the same parameters shown in Fig. 3 and consider a flowrate consisting of $Q_i(t)$ and a small perturbation $Q^\epsilon_i(t) = 0.2 Q_i(t) U(t)$, where Q_i is given in Fig. 3 and $U(t)$ is a bounded random perturbation in $[-1, 1]$. Figure 4 shows the pressure results and indicates the significant effect of the characteristic resistance on high-frequency oscillations in the RCR model, but not in the RC model. To mitigate the oscillatory influence, in the realistic applications as outflow boundary conditions, the ratio of the characteristic resistance R^i_{w1} to the total resistance R^i_w is relatively small, such as 0.056 for most outlets and a range of $0.1 - 0.2$ specifically for the renal and cerebral outlets within the full-body arterial network (Xiao et al. 2013; Xu et al. 2018). Figure 5 presents a comparison between the RC and RCR models. When α is sufficiently small, such as $\alpha = 0.056$, the difference between the two models is negligible. Even when α is not small (e.g., $\alpha = 0.2$), a proper adjustment of C_w in the RC model can still yield minor discrepancies in magnitude and phase compared with the RCR model. Such a small phase change is attributed to the temporal variation in flowrate in (11), as determined by the characteristic resistance.

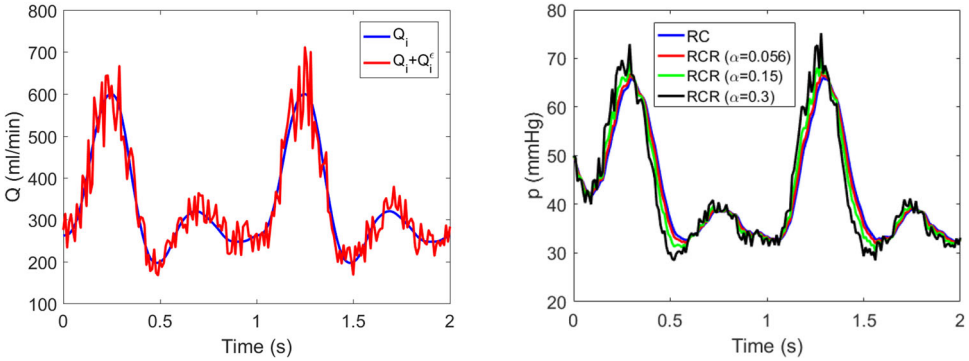

Fig. 4 High frequency oscillatory phenomenon observed in the RCR Windkessel model with an oscillatory flowrate Q and a suitable characteristic resistance, where $R_w = 10^4$, $R_{w1} = \alpha R_w$, $R_{w2} = (1-\alpha)R_w$, $C_w = 10^{-5}$, $p(0) = 50$mmHg. From left to right: (1) An artificial oscillatory flowrate Q; (2) Comparison of the pressure from RC and RCR models with different α

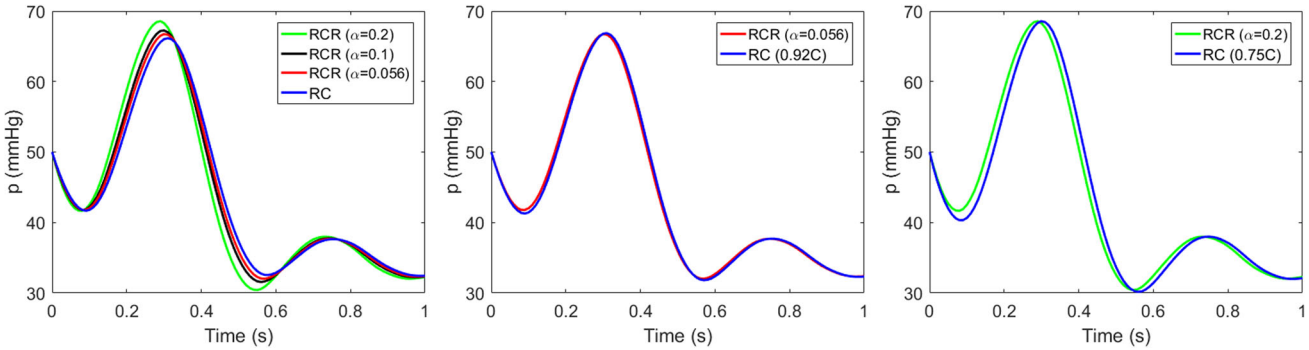

Fig. 5 A comparison of RC and RCR models with different characteristic resistances $R_{w1} = \alpha R_w (\alpha = 0.2, 0.1, 0.056)$, $R_{w2} = R_w - R_{w1}$. Left to right: (1) RC and RCR models use the same capacitance; (2) The capacitance in the RC model is 92% of that in the RCR model with $\alpha = 0.056$; (3) The capacitance in the RC model is 75% of that in the RCR model with $\alpha = 0.2$

2.4 Stabilized finite element discretization

Consider Sobolev spaces

$$\boldsymbol{V}^0 = \{\boldsymbol{u} \in \boldsymbol{H}^1(\Omega) : \boldsymbol{u}|_{\Gamma_I \bigcup \Gamma_w} = \boldsymbol{0}\}, \quad W = L^2(\Omega).$$

and $\boldsymbol{V} = \{\boldsymbol{u} \in \boldsymbol{H}^1(\Omega) : \boldsymbol{u}|_{\Gamma_I} = \boldsymbol{u}_I, \boldsymbol{u}|_{\Gamma_w} = \boldsymbol{0}\}$. Denote the inner product as $(u, v) := \int_\Omega uv\mathrm{d}\Omega$ in the domain Ω and $(u, v)_\Gamma := \int_\Gamma uv\mathrm{d}\Gamma$ on the boundary Γ. Let $\mathcal{T}_h$ be a shape-regular unstructured tetrahedral mesh of Ω, and the continuous, piecewise linear polynomial function space on $\mathcal{T}_h$ is denoted by S_h. We define the finite element spaces $\boldsymbol{V}_h = [S_h]^3 \cap \boldsymbol{V}$, $\boldsymbol{V}_h^0 = [S_h]^3 \cap \boldsymbol{V}^0$ and $W_h = S_h \cap W$. To avoid the discrete inf-sup condition (Boffi et al. 2013), we use a stabilized finite element method introduced in Franca and Frey (1992) for the spatial discretization, and adopt the second-order backward differentiation formula (BDF2) for the temporal discretization, i.e., to find $(\boldsymbol{u}_h^n, p_h^n) \in \boldsymbol{V}_h \times W_h$ such that

$$\begin{aligned}
&\left(\rho D\boldsymbol{u}_h^n, \boldsymbol{v}_h\right) + (\rho \boldsymbol{u}_h^n \cdot \nabla \boldsymbol{u}_h^n, \boldsymbol{v}_h) \\
&\quad + (\mu \nabla \boldsymbol{u}_h^n, \nabla \boldsymbol{v}_h) - (p_h^n, \nabla \cdot \boldsymbol{v}_h) + (q_h, \nabla \cdot \boldsymbol{u}_h^n) \\
&\quad + \sum_{K \in \mathcal{T}_h} \left(\rho\left(D\boldsymbol{u}_h^n + \boldsymbol{u}_h^n \cdot \nabla \boldsymbol{u}_h^n\right) + \nabla p_h^n, \gamma_1(\boldsymbol{u}_h^{n-1} \cdot \nabla \boldsymbol{v}_h + \nabla q_h)\right)_K \\
&\quad + \sum_{K \in \mathcal{T}_h} \left(\nabla \cdot \boldsymbol{u}_h^n, \gamma_2 \nabla \cdot \boldsymbol{v}_h\right)_K - (\mu \nabla \boldsymbol{u}_h^n \cdot \boldsymbol{n}, \boldsymbol{v}_h)_{\Gamma_O} + (g_h^n, \boldsymbol{v}_h \cdot \boldsymbol{n})_{\Gamma_O} \\
&\quad = 0, \ \forall (\boldsymbol{v}_h, q_h) \in \boldsymbol{V}_h^0 \times W_h
\end{aligned} \tag{13}$$

for any $t^n = n\Delta t$ with stabilization parameters γ_1 and γ_2, where $D\boldsymbol{u}_h^n$ denotes the first-order ($n = 1$) or second-order ($n \geq 2$) approximation of $\partial \boldsymbol{u}_h / \partial t$ at t^n. The outlet boundary integral term $(g_h^n, \boldsymbol{v}_h \cdot \boldsymbol{n})_{\Gamma_O}$ in (13) is obtained by discrete schemes for the RC Windkessel BC. Specifically, we adopt a semi-explicit time integration scheme (Grinberg and Karniadakis 2008) for (7)

$$p_h^n = \frac{R_w^i C_w^i}{R_w^i C_w^i + \Delta t} p_h^{n-1} + \frac{R_w^i \Delta t}{R_w^i C_w^i + \Delta t} Q_{i,h}^{n-1}, \quad i = 1, \ldots, m, \tag{14}$$

to obtain an approximation of $p(t^n)$ as the outlet pressure, where $Q_{i,h}^{n-1} = \int_{\Gamma_O^i} \boldsymbol{u}_h^{n-1} \cdot \boldsymbol{n} \mathrm{d}\Gamma_O^i$ is the discrete approximation of $Q_i(t^{n-1})$.

2.5 Newton-Krylov algorithm with an efficient two-level additive Schwarz preconditioner

Let us rewrite the corresponding nonlinear system of (13) as

$$F^n(X^n) = 0, \tag{15}$$

where X^n is the unknown vector. To solve the large, sparse, and nonlinear system (15) at each time step, we introduce a highly efficient and scalable Newton-Krylov-Schwarz (NKS) algorithm in which a two-level additive Schwarz preconditioner with a centerline-based coarse preconditioner (Liu and Cai 2023; Liu et al. 2023a, b) is employed. The details of this algorithm are described in Liu et al. (2023a). Let X_0^n be the initial guess, obtained from the solution at the previous time step X^{n-1} and let X_k^n denote the current approximate solution of X^n at the kth Newton step. At each Newton step, compute the Jacobian matrix J_k^n of F^n at X_k^n and then solve the following right preconditioned Jacobian system with the generalized minimal residual method (GMRES)

$$J_k^n \left(M_k^n\right)^{-1} M_k^n s_k^n = -F^n(X_k^n) \tag{16}$$

to determine the Newton direction s_k^n, where $(M_k^n)^{-1}$ is a two-level additive Schwarz preconditioner introduced as follows. First, we divide the computational domain into np nonoverlapping subdomains $\Omega_i, i = 1, 2, \cdots, np$, ensuring each subdomain aligns with the mesh $\mathcal{T}_h$, where np denotes the number of subdomains. Then, by adding δ layers of elements from neighboring subdomains of Ω_i, we extend Ω_i to form the overlapping subdomain Ω_i^δ, where δ represents the number of overlap layers, as shown in Fig. 6. Define the restriction operators R_i^0 and R_i to map the global vector defined in the whole domain Ω to the local vector defined on the nonoverlapping subdomain Ω_i and the overlapping subdomain Ω_i^δ, respectively. Following the centerline-based coarse preconditioners for normal arteries (Liu and Cai 2023; Liu et al. 2023a) and abnormal arteries (Liu et al. 2023b), we implement a two-level restricted additive Schwarz preconditioner

$$(M_k^n)^{-1} = \sum_{i=1}^{np} (R_i^0)^T (J_{k,i}^n)^{-1} R_i + E_c (J_{k,c}^n)^{-1} R_c, \tag{17}$$

where $J_{k,i}^n$ is the subdomain matrix of the Jacobian matrix J_k^n on the ith overlapping subdomain, $J_{k,c}^n$ is the corresponding Jacobian matrix of a centerline-based coarse problem introduced in Liu et al. (2023a, b), R_c and E_c are restriction and extension matrices between the coarse and fine finite element spaces, respectively.

3 Results and discussion

In this section, we present numerical experiments on renal arteries to study blood flow features and the impact of the outflow BCs under different vascular conditions, including a normal case (Case I), a stenotic case (Case II), and an aneurysmal case (Case III), shown in Fig. 1. We set the density $\rho = 1.0\text{g/cm}^3$, the viscosity $\mu = 0.035\text{g/(cm·s)}$, and the cardiac cycle $T = 1.0\text{s}$ in the simulations. For the three outlet pressure BCs, Table 1 lists the corresponding prescribed parameter values for these cases. For the constant pressure BC, a constant pressure of 90mmHg is set for all cases, representing the mean pressure derived from a physiological systolic blood pressure of 120mmHg and diastolic blood pressure of 80mmHg. For the resistance BC, the total resistance is obtained to approximately match the systolic pressure of 120mmHg. For the Windkessel BCs, the total resistance and capacitance parameters are configured to maintain the numerical pressures within the above physiological range. Specifically, these parameters are first initialized using the corresponding 0D model and then iteratively optimized based on 3D simulation results. A stabilized P1-P1 finite element method combined with the BDF2 is employed for discretization. Unstructured meshes with a mesh size of about 0.2mm and a time step size of $\Delta t = 0.01\text{s}$ are used in the model discretization. The resulting nonlinear system, with over one million degrees of freedom, is solved using the NKS algorithm. To ensure stable numerical results, each simulation is run for three cardiac cycles, with the following results reported for the third cycle.

3.1 Convergence analysis and algorithm performance

We first perform sensitivity analyses on both the mesh and time step to verify the accuracy of the numerical solution. We consider Case I with the Windkessel BC for three unstructured meshes: Mesh 1, Mesh 2, and Mesh 3 with $9.65 \cdot 10^5$, $2.16 \cdot 10^6$ and $4.35 \cdot 10^6$ tetrahedral elements, respectively, shown in Fig. 7 for the details. Figure 8 shows the numerical pressure and velocity curves in a cardiac cycle for these three meshes at two monitoring points located near the first branch (the left subfigures) and an outlet (the right subfigures). For the pressure curves, we can see that the coarsest mesh (Mesh 1) yields sufficiently accurate results compared with the finest one (Mesh 3), with the error less than 0.1mmHg. For the velocity curves, the results show a gradual convergence as the mesh is refined. In this case, Mesh 2 yields results comparable to Mesh 3 and is used for subsequent hemodynamic analysis. To investigate the impact of the time step size Δt on the numerical accuracy, we test three time step sizes: 0.01s, 0.005s and 0.0025s. Fig. 9 shows the pressure variations over time at the two points mentioned

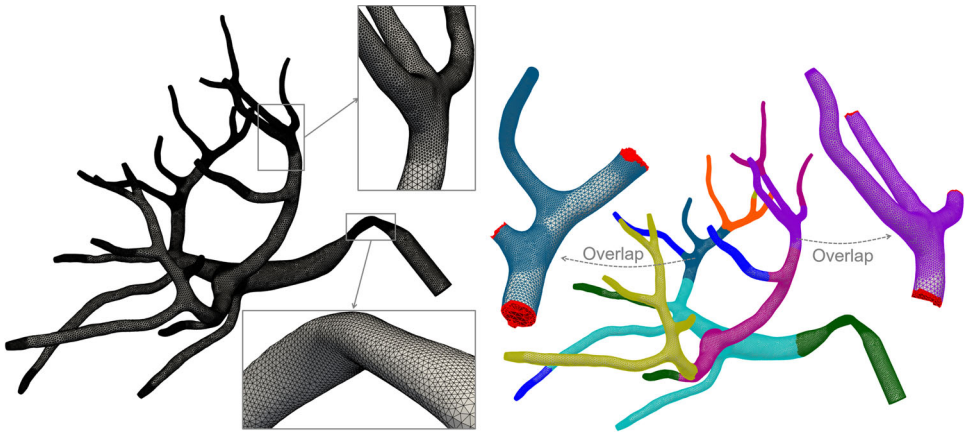

Fig. 6 An unstructured mesh of a stenotic renal artery and its non-overlapping partition with 10 subdomains, where the overlapping subdomains are generated by merging one layer of elements from adjacent subdomains

Table 1 Parameter values of three outflow boundary conditions in three renal arterial cases

Outflow BC	Parameter	Case I	Case II	Case III
Constant	p_c (mmHg)	90.00	90.00	90.00
Resistance	R_r (dyn · s · cm^{-5})	$5.00 \cdot 10^3$	$6.55 \cdot 10^3$	$3.40 \cdot 10^3$
Windkessel	R_w (dyn · s · cm^{-5})	$2.45 \cdot 10^4$	$5.48 \cdot 10^4$	$1.60 \cdot 10^4$
	C_w (cm^5 · dyn^{-1})	$1.47 \cdot 10^{-5}$	$2.10 \cdot 10^{-5}$	$2.93 \cdot 10^{-5}$

above. The results show that decreasing the time step from 0.01s to 0.0025s increases accuracy, but the relative error at systole is already below 2%, suggesting only minimal further improvement. Table 2 shows the performance of the algorithm with the two-level Schwarz preconditioner in terms of the number of linear iterations, compared with the classical one-level Schwarz preconditioner. For all tested cases with different meshes and cardiac cycle phases, the two-level method exhibits a significant reduction in linear iterations compared with the one-level method, indicating the robustness and effectiveness of the algorithm.

3.2 Case I: a normal renal artery

In the first case, we consider a normal renal artery. In patient-specific hemodynamic simulations, the inflow velocity or inflow rate can be obtained from clinical measurements such as Doppler ultrasound and Phase-Contrast MRI (Morbiducci et al. 2013; Mariotti et al. 2023). Considering the lack of clinical inlet data in this study, the inflow velocity waveform from Taylor et al. (1998) is prescribed in the following numerical simulations. Before we focus on the impact of outflow BCs, we first investigate the effect of the inlet velocity profile on the numerical results. We compare plug and parabolic profiles with the same inflow rate as the inlet BC, and Fig. 10 shows the velocity profiles and average pressure at cross sections located 1, 3, 6, 9, and 11 diameters distal to the inlet at the peak systole. The impact of the velocity profile on the numerical results is small beyond suitable diameters distal to the inlet, consistent with Madhavan and Kemmerling (2018) for aortic arteries and Moyle et al. (2006) for carotid arteries. The average pressure for the parabolic profile is about 0.5mmHg higher compared with the plug profile and the change in pressure drop is insignificant.

Next, we focus on the effect of outflow BCs. Fig. 11 shows the distributions of the streamline, velocity magnitude, and pressure for three outflow BCs at the peak systole. The streamline aligns with the arterial path, indicating a typical flow pattern. The outflow BCs affect the blood flow of branches, especially near the outlets. Compared with the constant BC, the velocity profile at a cross section obtained from the resistance BC more closely approximates that of the Windkessel BC. The pressure distribution at the peak systole differs markedly, owing to the different outflow pressure BCs. Fig. 12 shows the pulsatile pressure curves over a cardiac cycle at three points—located at the inlet (A), the first bifurcation (B), and an outlet (C)—along with the pulsatile flux curve at a cross section near an outlet for three BCs. The decrease in pressure from A (inlet) to C (outlet) can be observed. The constant pressure BC yields an unreasonable pressure waveform with a small amplitude from the prescribed outlet pressure of 90mmHg (Vignon-Clementel et al. 2006). The resistance BC offers a pressure waveform with an excessively high amplitude, and it causes in-phase pressure and flux curves (Reymond et al. 2009). In contrast, the Windkessel BC generates a physiologically realistic pressure waveform, with a range of approximately 82-118mmHg, and exhibits a phase lag between pressure and flux curves, consistent with findings in Vignon-Clementel et al. (2006) for carotid arteries. Moreover, the outflow rate curves for the

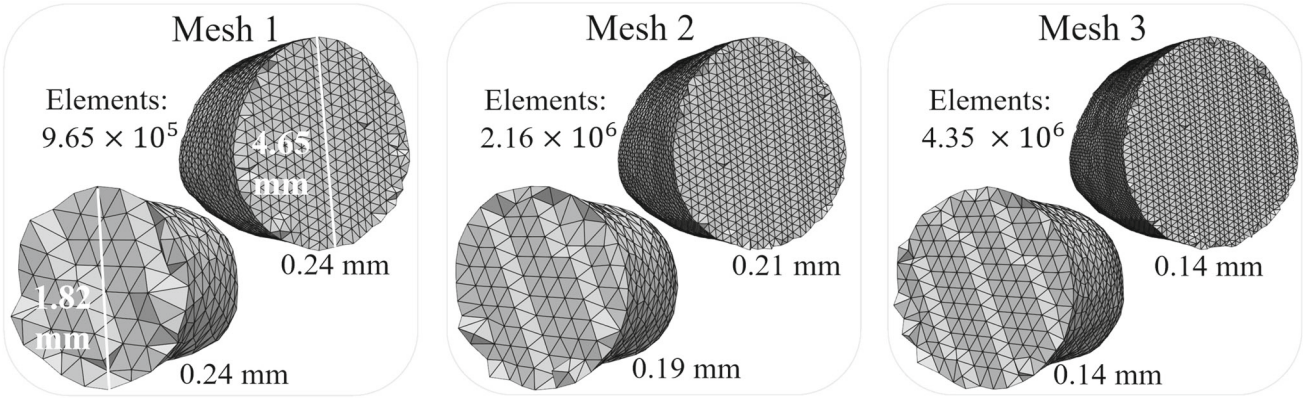

Fig. 7 Mesh details near the inlet (top) and outlet (bottom) regions for Case I. The mesh size globally decreases from 0.24mm to 0.14mm

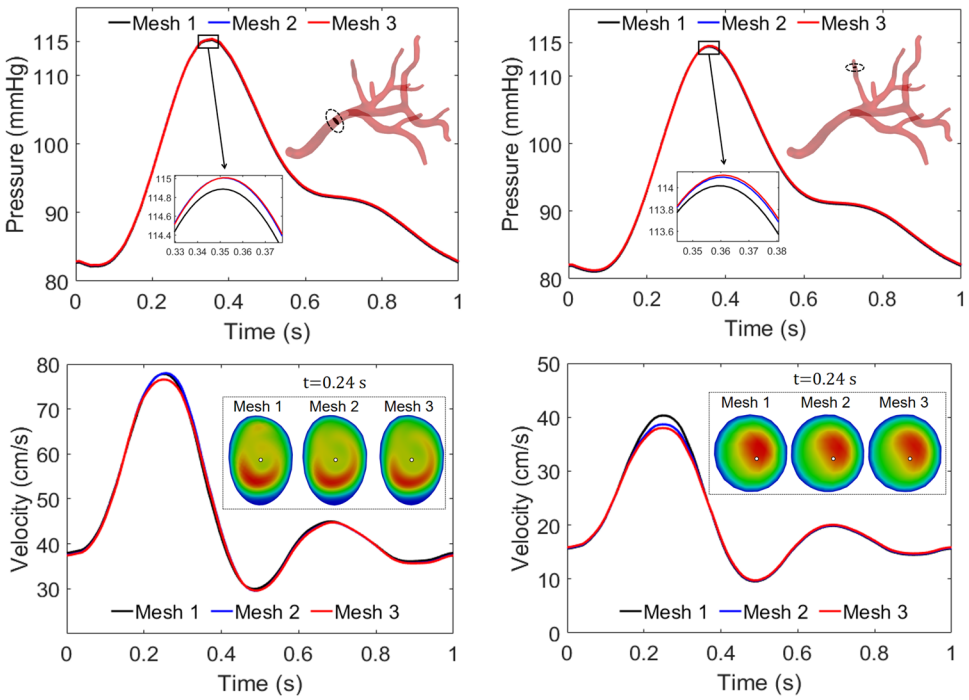

Fig. 8 Mesh sensitivity analysis in Case I: Pressure (top) and velocity (bottom) variations over a cardiac cycle for three meshes at two monitoring points near the first branch (left) and outlet (right), respectively, where the local velocity profiles on the corresponding cross section are shown

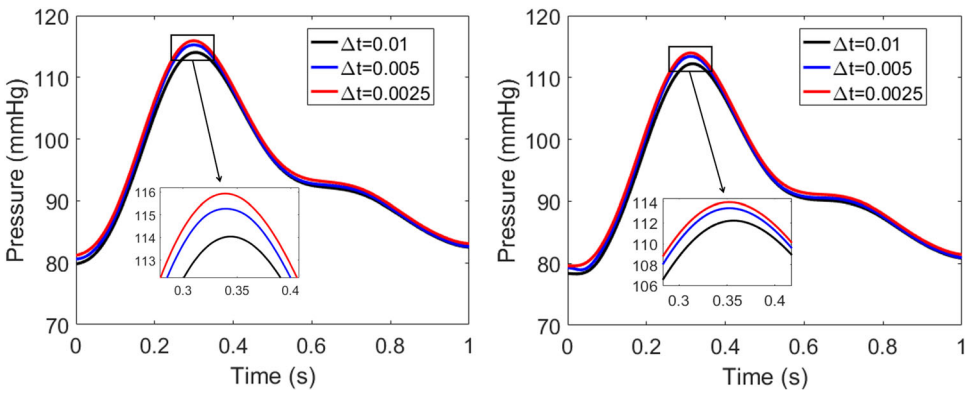

Fig. 9 Time-step sensitivity analysis in Case I: Impact of the time-step size Δt in a cardiac cycle on the numerical pressure at two points mentioned in Fig. 8

Table 2 Performance comparison of the NKS algorithm with the one-level and two-level preconditioners, where *np* is the number of subdomains, 'NI' is the number of Newton iterations, 'LI1' and 'LI2' are the average numbers of linear iterations per Newton step for the one-level and two-level preconditioners

Mesh	*np*	NI	$t = 0.12$ s		$t = 0.24$ s		$t = 0.36$ s		$t = 0.48$ s	
			LI1	LI2	LI1	LI2	LI1	LI2	LI1	LI2
Mesh 1	64	2	275.0	45.0	306.0	43.5	216.0	46.5	251.0	26.5
	128	2	278.5	45.5	310.0	44.0	195.5	47.5	245.5	27.0
Mesh 2	128	2	461.5	59.5	584.0	59.5	385.5	63.0	353.0	34.0
	256	2	483.5	60.5	583.5	60.0	397.0	64.0	403.5	34.5
Mesh 3	256	2	512.0	77.0	600.0	78.0	489.5	82.0	521.5	42.0
	512	2	519.0	78.5	600.0	80.0	421.0	83.0	521.0	43.0

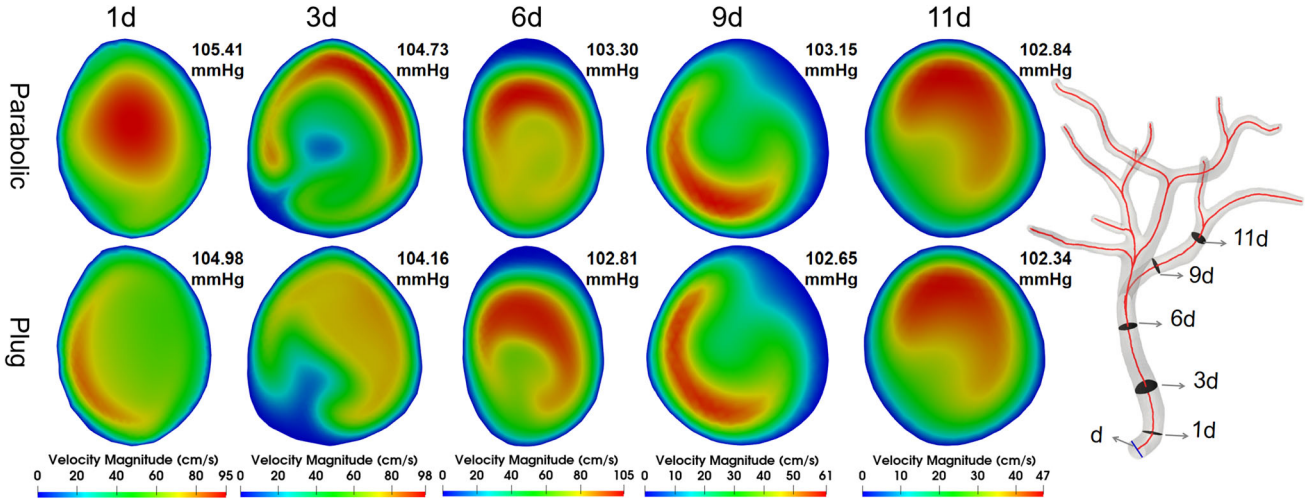

Fig. 10 Comparison of the parabolic (top) and plug (bottom) inlet profiles for Case I: Velocity distributions at cross sections located $1d$, $3d$, $6d$, $9d$ and $11d$ distal to the inlet at the peak systole, where d is the diameter of the inlet and the average pressure on each cross section is marked

resistance and Windkessel BCs are nearly identical. These observations for the normal renal artery demonstrate that the choice of outflow BCs remarkably impacts the numerical velocity and pressure, with the Windkessel BC producing more physiologically accurate results than the constant and the resistance BCs.

To investigate the impact of the characteristic resistance on the hemodynamic result, we numerically compare the RC and RCR Windkessel models with the proximal resistance ratio $\alpha = 0.1$ in this case. Figure 13 compares the pressure waveform and the flow rate over a cardiac cycle. We first observe that the velocity distributions and flow rates are nearly identical for the two models, indicating that velocity-based hemodynamic factors, such as WSS and OSI, are not affected by the characteristic resistance. The pressure waveforms for the two models, however, exhibit some discrepancies, which can be reduced by tuning the capacitance from C_w to $0.78C_w$, with a small phase shift of 0.03s. The peak pressure distribution obtained with the RC model is markedly improved after adjustment relative to the RCR result. The time-averaged pressures at the inlet are 95.56mmHg (RCR with C_w), 95.60mmHg (RC with C_w), and 95.51mmHg (RC with $0.78C_w$), which shows a minor difference of less than 0.05mmHg. This suggests that the impact on time-averaged pressure-based hemodynamic factors, such as rFFR and PD, is negligible. In the following cases, we focus on patient-specific abnormal renal arteries to characterize their hemodynamic behavior and indicators, and to evaluate the impact of these outflow BCs on these parameters.

3.3 Case II: a stenotic renal artery

In this case, a renal artery with an 87% area stenosis is present near the inlet, shown in Fig. 14. Fig. 15 shows the global distributions of the pressure and the velocity magnitude at peak systole for the Windkessel BC. The pressure exhibits a rapid decrease near the stenosis and a complex flow pattern occurs behind the stenotic region. In the downstream of the stenosis, we observe both regions of low and high WSS on opposing sides of the arterial wall, with the inner side corresponding to low WSS (Asakura and Karino 1990). The cross-sectional flow visualization reveals that these areas frequently exhibit vortices with bidirectional flow, resulting in an oscillatory WSS pattern. These hemodynamic conditions—low and oscillatory WSS—play a critical role in

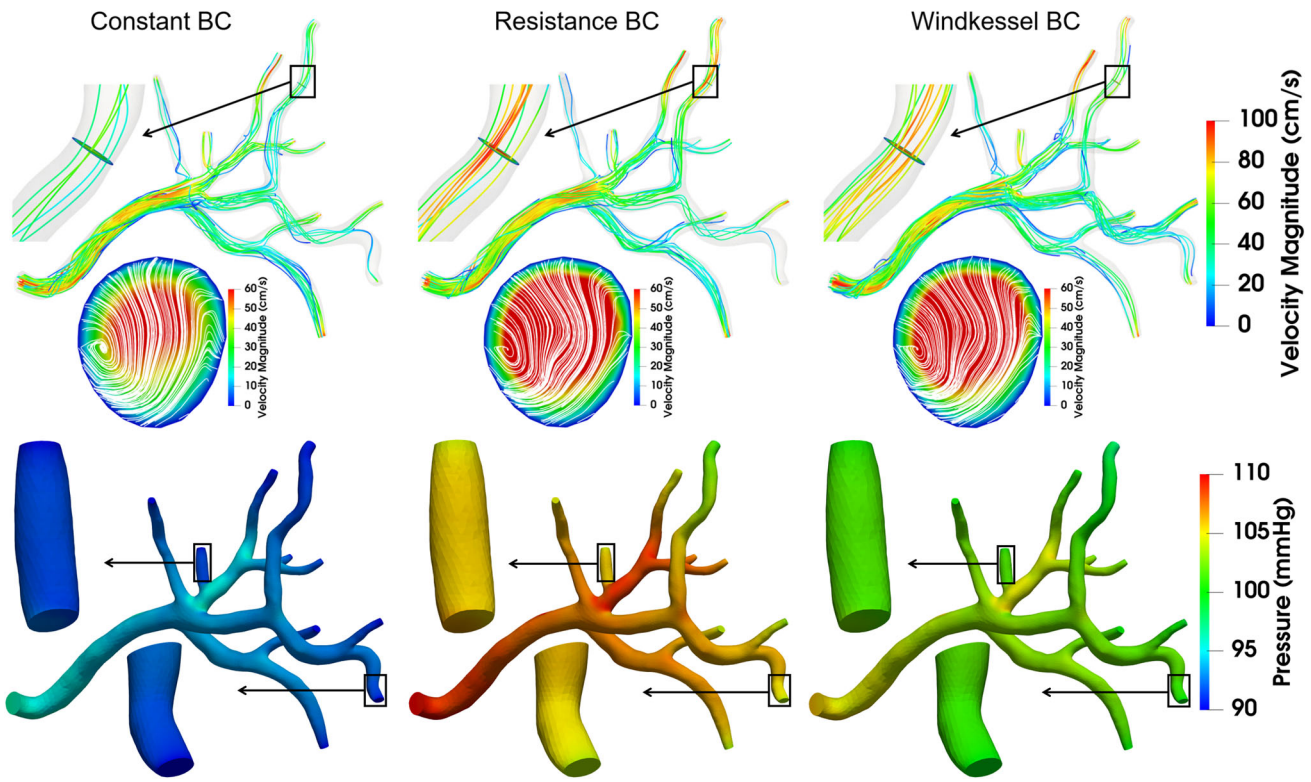

Fig. 11 Case I: Distributions of the streamline and pressure at peak systole for three outflow boundary conditions

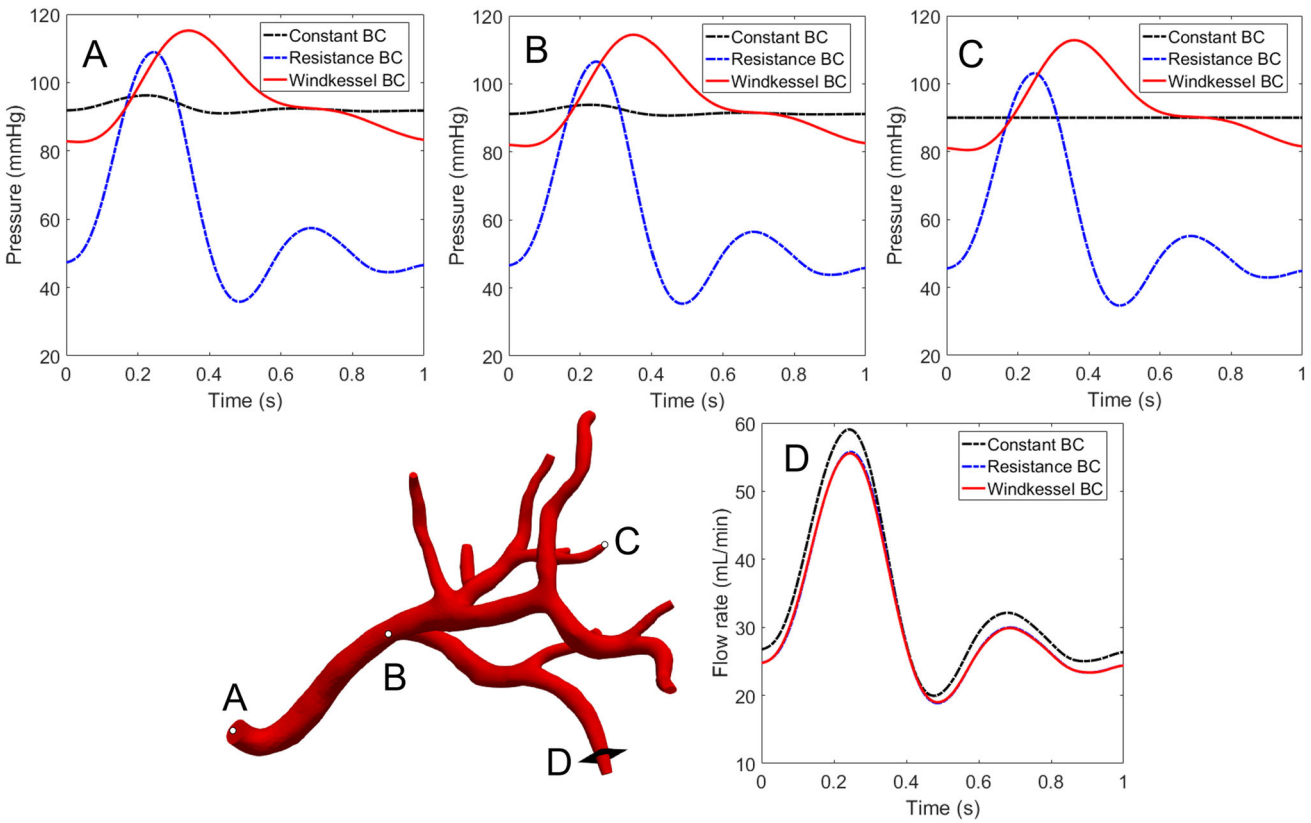

Fig. 12 Case I: Comparisons of pressure curves at points A (inlet), B (bifurcation), and C (outlet), and flux curves on the cross section D (near outlet) for three outflow boundary conditions

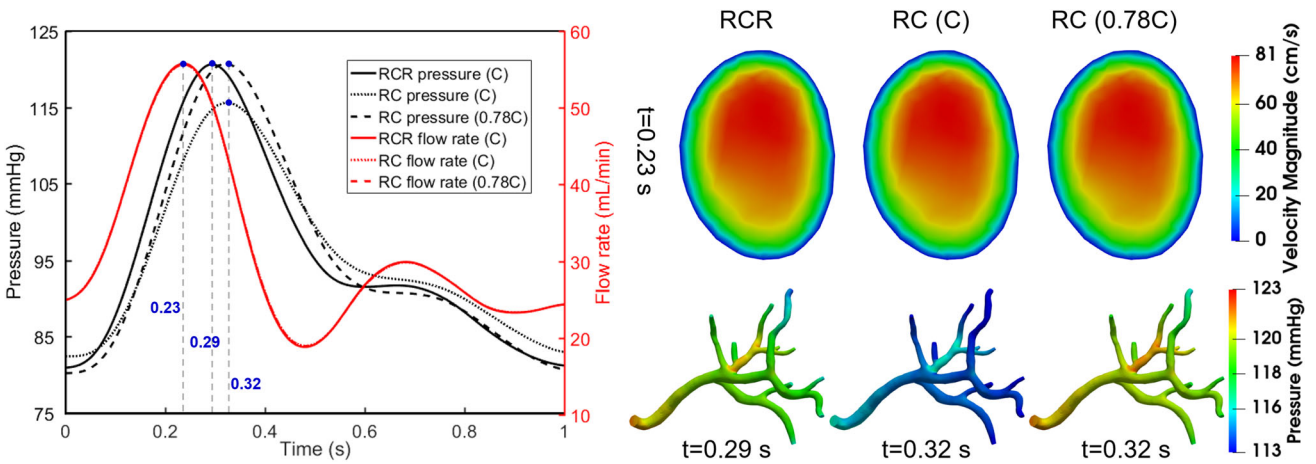

Fig. 13 Comparison of the RC and RCR Windkessel models for Case I: Pressure waveform at point A and flow rate on cross section D over a cardiac cycle (left), as marked in Fig. 12; velocity distributions on cross section D (top right) and global pressure distributions (bottom right)

driving atherosclerotic plaque formation (Malek et al. 1999). Figure 16 shows the local features in the stenotic region for three outflows BCs. The pressure distributions are significantly different among the three BCs, whereas the velocity distributions are almost the same. However, as shown in Fig. 17, the velocity profiles are parabolic-like, but obvious velocity differences are observed near the outlet highlighted in red in Fig. 14. This suggests that the outflow BC notably affects the hemodynamic results near the outlets. To quantify the influence of outflow BCs on the outflow rate, we compute the mean outflow ratios for all outlets over a cardiac cycle, expressed as a percentage of the total outflow rate, as shown in Fig. 18. The relative errors are below 2.6% for the resistance and Windkessel BCs, but up to 61% at certain outlets for constant pressure and Windkessel BCs. The resistance and Windkessel BCs produce almost similar outflow rate distributions, owing to their highly related formulations. These outflow ratios correspond closely to the outlet area ratios, determined by the 3/2 power of the outlet areas (the black bar), consistent with the definition of the resistance and Windkessel BCs. Conversely, the constant pressure BC governs outflow rates through a fixed outlet pressure, leading to remarkable differences in certain branches compared with the resistance and Windkessel BCs.

To further study the influence of these BCs on risk hemodynamic indicators. We consider two commonly used indicators: rFFR (Subramanian et al. 2005) and PD (Yim et al. 2004; Andayesh et al. 2020). The rFFR is defined as the ratio of the maximum blood flow in the presence of stenosis to the maximum flow in its absence. In clinical practice, a pressure guidewire is used to assess the hemodynamics by measuring the time-averaged proximal pressure $\bar{P}_a$ (upstream of the stenosis) and the time-averaged distal pressure $\bar{P}_d$ (downstream of the stenosis) in the hyperemic state. The rFFR and PD are calculated as

$$\text{rFFR} = \frac{\bar{P}_d}{\bar{P}_a}, \quad \text{PD} = \bar{P}_a - \bar{P}_d, \tag{18}$$

providing quantitative measures of the functional severity of the stenosis. Instead of using the invasive method, these pressure values can be computed approximately and numerically. According to the standard clinical protocol (Mandaltsi et al. 2018), the proximal pressure is measured as far as possible from the stenosis, near the aortic opening, while the distal pressure is measured 10–20 mm downstream of the stenosis. Following the protocol, we designate three downstream cross sections and compute the average pressure across these cross sections, shown in Fig. 14. Table 3 presents the proximal and the distal pressures of the stenosis, and the corresponding numerical rFFR and PD values, for three outflow BCs. We observe that the numerical rFFR is comparable between the constant and Windkessel BCs but diverges from that obtained with the resistance BC as the time-averaged proximal and distal pressures are significantly lower than a physiological range. However, the PD values are identical, which are not affected by the outflow BCs. This phenomenon is similar to the velocity field shown in Fig. 16, which implies that the PD is a more reliable indicator for associating with the flow rate numerically. In fact, the RAS typically activates pressure autoregulation, leading to systemic Goldblatt hypertension, which is determined by the pressure drop (Andayesh et al. 2020). According to Yim et al. (2004), a mean pressure drop of at least 10mmHg or a peak pressure drop of at least 20mmHg is considered hemodynamically significant. The indicator rFFR is actually strongly and significantly correlated with the time-averaged pressure drop PD, rather than with angiographic diameter stenosis, which was observed by Subramanian et al. (2005). Moreover, De Bruyne et al. (2006) found that the pressure ratio $\bar{P}_d/\bar{P}_a$ below 0.9 likely induces the renovascular hypertension.

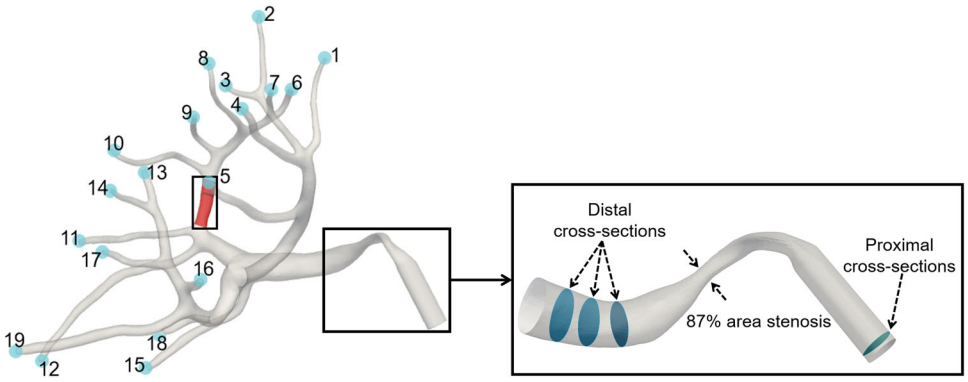

Fig. 14 Case II: A stenotic renal artery with 19 outlets, with one proximal and three distal cross sections are chosen for calculating the average proximal and distal pressures

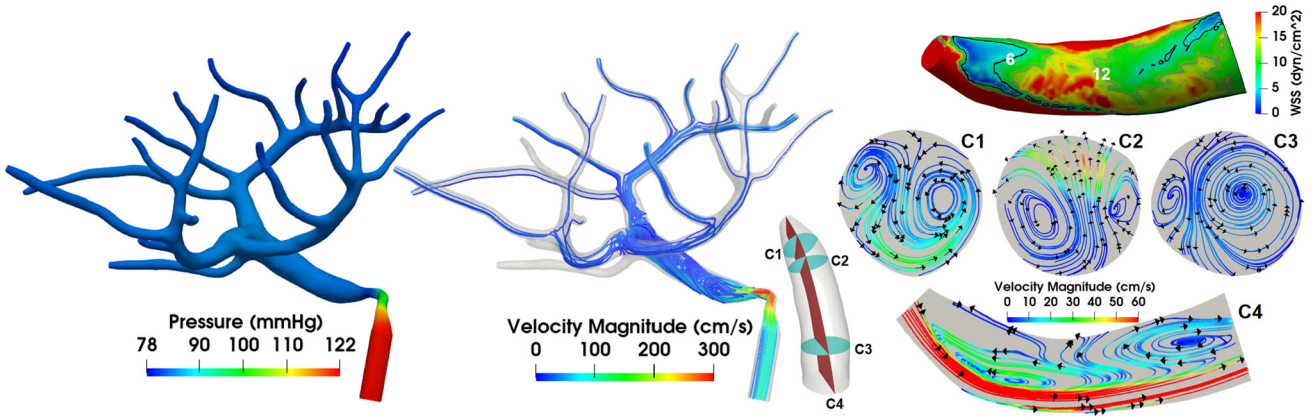

Fig. 15 Case II: Global distributions of pressure (left) and velocity (middle) magnitude at peak systole for the Windkessel boundary conditions. The local features (right) in the downstream of the stenosis are shown, including the WSS with contour and cross-sectional flow patterns

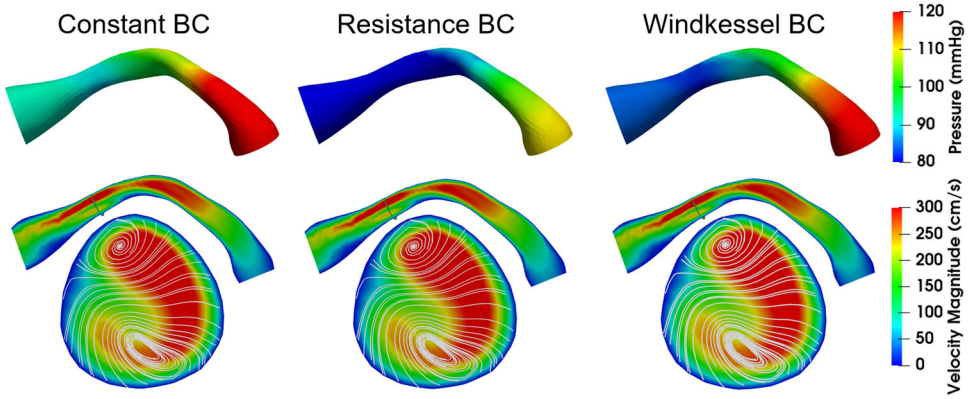

Fig. 16 Case II: Comparisons of the pressure (top) and velocity magnitude (bottom) in the stenosis at peak systole for three Outflow boundary conditions

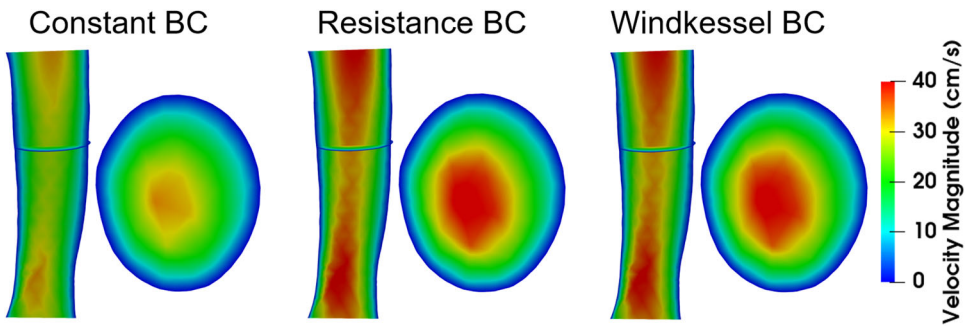

Fig. 17 Case II: Distributions of velocity magnitude near an outlet (marked in red in Fig. 14) for three outflow boundary conditions

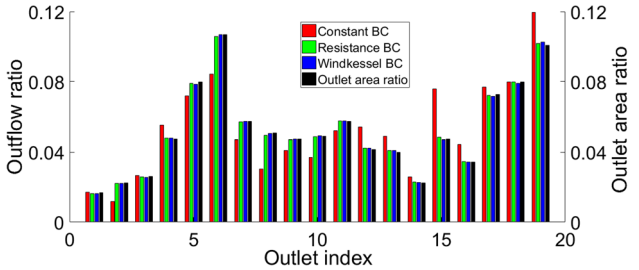

Fig. 18 Case II: Mean outflow ratios and outlet area ratios of all nineteen outlets for three outflow boundary conditions, where the outlet area ratios are computed by $S_i^{\frac{3}{2}} / \left(\sum_{i=1}^{m} S_i^{\frac{3}{2}} \right)$ with the outlet areas $\{S_i\}_{i=1}^{m}$

Note that the resistance of the downstream vascular network is affected by the autoregulation mechanism (Collard et al. 2020). To investigate the sensitivity of the resistance for the Windkessel BC, we introduce a parameter to change it, i.e., $(1+\beta)R_w$. Table 3 also shows the numerical rFFR and PD for different resistances. The rFFR demonstrates low sensitivity, showing a variation of less than 3% even when the resistance changes by over 20%. The pressure drop remains almost constant regardless of the change in resistance. However, the proximal and distal pressures change obviously, as shown in Fig. 19. Furthermore, the flow rate near the first bifurcation is insensitive to variations in the resistance (detailed numerical results not shown). The insensitivity phenomenon in pressure drop for the resistance is not consistent with the observation in Mariotti et al. (2023) for the aorta with coarctation. In Mariotti et al. (2023), the impact of the outflow BC on the pressure drop is justified as the outlet is near the lesion, especially for a severe coarctation. This phenomenon appears to be dependent on the lesion location, and the distal includes rich branches and the outlets are far from the lesion.

3.4 Case III: an aneurysmal renal artery

In this case, we focus on a patient-specific geometry that comprises an abdominal aortic segment along with the bilateral renal arterial networks. The right renal artery has a 13.3mm saccular aneurysm located at the renal hilum. For the simulation, we prescribe a velocity Dirichlet BC at the abdominal aortic outlet, allocating 81% of the total flow rate to guarantee that 19% of the total flow rate is directed to the kidneys via the left and right renal arteries (Valentin 2002). For the remaining outlets in the renal arteries, we implement one of three outflow BCs. Fig. 20 shows the distributions of velocity magnitude and pressure. Flow patterns in the abdominal region are similar, but they exhibit distinct differences in the aneurysm and the left and right small branches. The pressure from the resistance BC exceeds that of the constant pressure and Windkessel BCs. Fig. 21 presents the outflow ratio distributions at the abdominal aortic outlet, the left and right renal arteries. The outflow ratio difference between the left and right renal arteries is 0.006 for both the resistance and Windkessel BCs, leading to around a 6% difference in outflow rates. However, the constant pressure BC causes a difference of 0.02, corresponding to approximately a 20% difference in the outflow rates between the left and right renal arteries. Such an asymmetric outflow pattern has been previously observed in an abdominal aortic bifurcation (Vignon-Clementel et al. 2006).

To investigate the hemodynamics within the aneurysm, we compute two WSS-based hemodynamic indicators: the time-averaged WSS (TAWSS) (Di Achille et al. 2014) and OSI, which characterize the magnitude and oscillatory degree of the blood flow shear stress on the aneurysmal wall, respectively. The WSS is defined as the tangential vector of the normal stress tensor (Kong et al. 2018) on the aneurysm region, and these indicators are given by

$$\text{TAWSS} = \frac{1}{T}\int_0^T |\text{WSS}|dt, \quad \text{OSI} = \frac{1}{2}\left(1 - \frac{|\int_0^T \text{WSS}dt|}{\int_0^T |\text{WSS}|dt}\right). \tag{19}$$

Fig. 22 shows TAWSS and OSI on the aneurysm wall under different outflow BCs. The distributions of TAWSS are largely consistent across the different outflow BCs. In contrast, the high OSI on the aneurysmal body and dome under the resistance BC differs distinctly from that observed under the other two BCs, which indicates that the outflow BCs can still affect the flow patterns within the aneurysm even if the outlets are far away from the lesion.

The significant association between RAAs and hypertension is evidenced not only by the high prevalence of hypertension (70–100%) in large RAA patient cohorts (Zhang et al. 2023; Klausner et al. 2015; Coleman and Stanley 2015), but also by the observation that surgical repair improves or cures hypertension in the majority of cases (Coleman and Stanley 2015), suggesting a direct pathophysiological link. Down et al. observed, based on numerical simulations, that an aneurysm could cause flow distortions that led to higher than normal pressure losses. To analyze the effect of the aneurysm on the flow patterns and pressure in this case, we artificially remove the aneurysm and observe the change in hemodynamics. Fig. 23 presents a comparison of the velocity profiles, WSS, pressure and streamlines in the region surrounding the aneurysm. Following virtual aneurysm removal, WSS changes and increases in the specified local regions, and the velocity profiles at two downstream cross-sections are altered. The flow streamline patterns revert to a more normalized configuration. A significant pressure drop is observed across the region with an abrupt diameter change from upstream to downstream–a morphological alter-

Table 3 Case II: Comparisons of computed proximal and distal pressures, the renal fractional flow reserve and the pressure drop for three outflow boundary conditions, where the parameter β represents the relative change such that the resistance becomes $(1+\beta)R_w$

Outflow BC	Proximal pressure $\bar{P}_a$ (mmHg)	Distal pressure $\bar{P}_d$ (mmHg)	rFFR $\bar{P}_d/\bar{P}_a$	PD $\bar{P}_a - \bar{P}_d$
Constant	106.12	91.27	0.86	14.85
Resistance	55.54	40.69	0.73	14.85
Windkessel ($\beta = 0$)	96.65	81.80	0.85	14.85
Windkessel ($\beta = -0.18$)	83.03	68.18	0.82	14.85
Windkessel ($\beta = 0.22$)	111.58	96.74	0.87	14.84

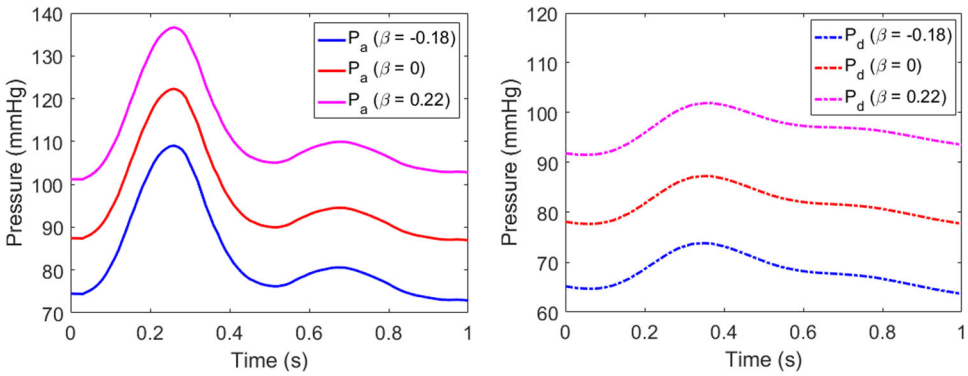

Fig. 19 Case II: Impact of the resistance parameter in the Windkessel BC on the proximal (left) and distal (right) pressures, where the adjusted resistance, given by $(1+\beta)R_w$, varies with β

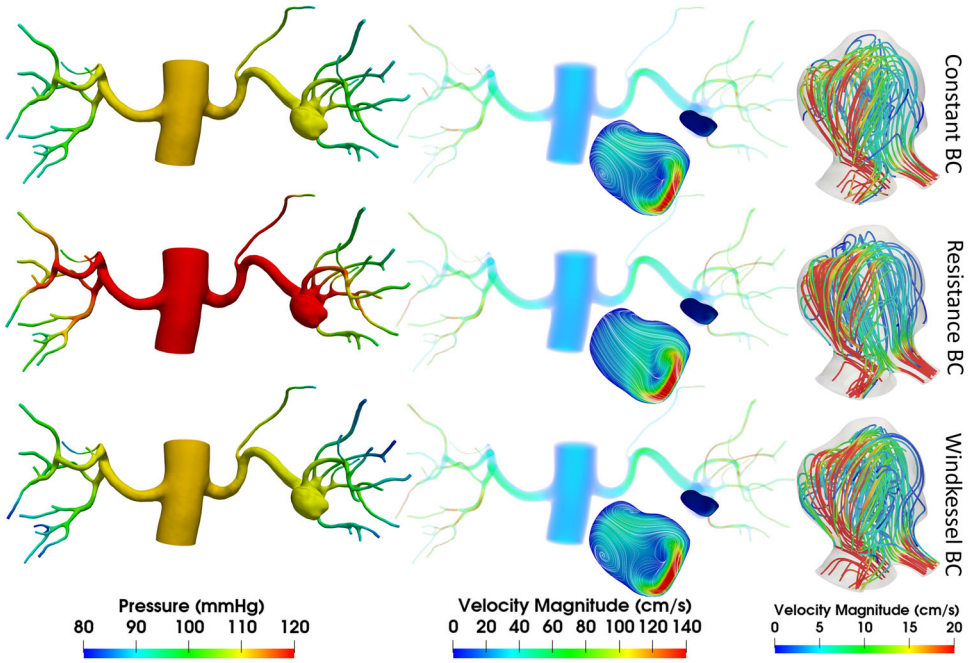

Fig. 20 Case IV: Distributions of the pressure, velocity magnitude and local features for three outlet boundary conditions at the peak systole

ation likely resulting from long-term aneurysm presence and its impact on flow patterns; in some specific outlet branches, this pressure drop exceeds 10mmHg and the pressure ratio is below 0.9, likely inducing a renovascular (secondary) hypertension. Notably, the virtual reconstruction results in a global decrease in pressure. A considerable pressure drop, however, remains attributable to the residual abnormal geometry with a sharply tapered diameter distribution.

4 Limitations

One of the main limitations of this study is the absence of clinical inflow velocity and pressure data. By employing a prescribed inlet velocity waveform and suitable outlet parameters, our model nonetheless captures the essential features of renal blood flow and local hemodynamics within the lesion region, enabling an analysis of boundary condition impacts. Incorporating clinical data would refine

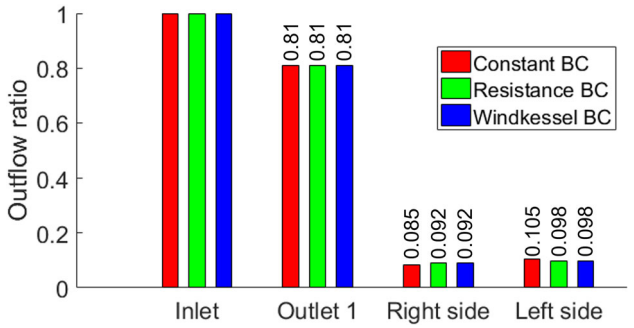

Fig. 21 Case IV: Distributions of time-averaged outflow ratios in the large abdominal aortic outlet (Outlet 1), the sum of total left (Left side) and right (Right side) renal outlets for three outlet boundary conditions

these boundary condition settings and enhance the personalization of hemodynamic analyses. Future work will therefore focus on acquiring more patient-specific renal arteries and corresponding boundary data to achieve more reliable hemodynamic analyses and predictions. Regarding model assumptions, while the use of Newtonian fluid fails to capture the non-Newtonian behavior of blood, prior studies indicate that its impact on flow distribution is typically not strong. Moreover, accounting for the elastic nature of the arterial wall would enhance model accuracy, it would also necessitate acquiring more patient-specific parameters, thereby increasing model complexity and data requirements. In such cases, inaccurate parameter specification may mean that numerical predictions are even worse than those from a pure fluid dynamics model.

5 Conclusions

CFD-based numerical simulations of blood flow in renal arteries with richly branching downstream vasculatures provide a non-invasive, high-fidelity method for obtaining hemodynamic results, enabling the computation of critical hemodynamic quantities, such as WSS, OSI, rFFR and PD, to assess the risk of individual renovascular diseases. Considering that measuring the outlet velocities or pressures is difficult due to the outlets of the renal arteries in computational models being embedded within the kidney tissue, a suitable outflow BC is essential for achieving accurate hemodynamic results. For this purpose, we evaluate the impact of three outflow BCs on renal hemodynamics. Numerical results indicate that the Windkessel BCs yield a more physiological pulsatile pressure distribution and reasonable outflow rate, compared with the constant pressure and resistance BCs. In terms of hemodynamic indicators for risk assessment within the lesions, the constant pressure BC yields values of TAWSS, OSI, rFFR, and PD that are comparable to those obtained with the Windkessel BC. This suggests that the constant pressure BC can be an effective and simplified modeling choice for capturing key hemodynamic features in certain renal artery structures when the focus is restricted to the lesion site. Furthermore, these hemodynamic details provide a basis for investigating the underlying progression mechanisms of vascular lesions and for improving risk assessment and prediction. In the case of severe renal artery stenosis, we observed a mean pressure drop exceeding 10mmHg and a significant reduction in rFFR (below 0.9). These significant hemodynamic alterations are clinically relevant and likely trigger renovascular hypertension. Similarly, renal aneurysms can induce complex downstream flow patterns, which may lead to abnormal vascular remodeling and also contribute to secondary hypertension. By providing a comprehensive hemodynamic analysis of renovascular diseases and evaluating the impact

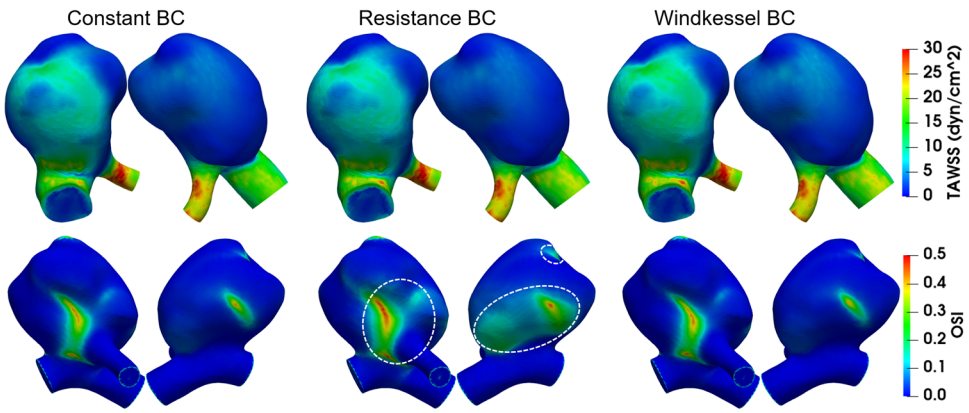

Fig. 22 Case III: Comparisons of the TAWSS and OSI on the aneurysmal wall for three outflow boundary conditions

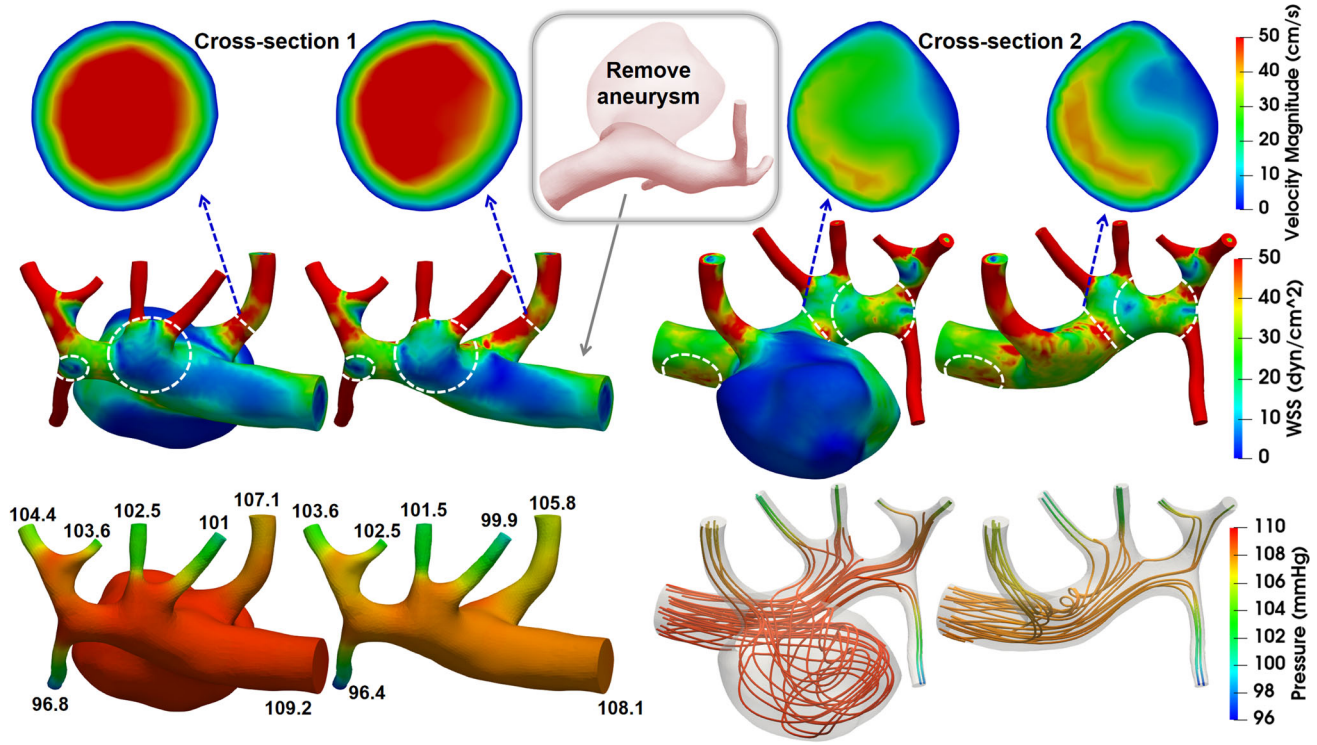

Fig. 23 Case III: Hemodynamics comparison before and after aneurysm removal at the peak systole under the Windkessel outflow boundary condition. The local features include velocity profiles on two downstream cross-sections adjacent to the aneurysm (top), WSS (middle), and pressure and streamline (bottom)

of outflow BCs, this study gives practical insights for renal artery simulations.

Acknowledgements This work was supported by FDCT 0146/2024/R1A2, 0135/2025/R1A2, 0084/2023/ITP2, MYRG GRG2025-00122-FST, and NSFC 12201658.

Author Contributions Fenfen Qi: Writing - original draft, Software, Methodology, Investigation, Data curation. Yingzhi Liu: Writing - original draft, Methodology. Rongliang Chen: Resources, Data curation. Xiao-Chuan Cai: Supervision, Methodology, Conceptualization.

Data availability No datasets were generated or analysed during the current study.

Declarations

Conflict of interest The authors declare no conflict of interest.

References

Andayesh M, Shahidian A, Ghassemi M (2020) Numerical investigation of renal artery hemodynamics based on the physiological response to renal artery stenosis. Biocybern Biomed Eng 40(4):1458–1468

Arzani A (2018) Accounting for residence-time in blood rheology models: do we really need non-Newtonian blood flow modelling in large arteries? J R Soc Interface 15(146):20180486

Asakura T, Karino T (1990) Flow patterns and spatial distribution of atherosclerotic lesions in human coronary arteries. Circ Res 66(4):1045–1066

Berg N, Fuchs L, Prahl Wittberg L (2019) Blood flow simulations of the renal arteries-effect of segmentation and stenosis removal. Flow Turbul Combust 102:27–41

Boccadifuoco A, Mariotti A, Celi S, Martini N, Salvetti M (2018) Impact of uncertainties in outflow boundary conditions on the predictions of hemodynamic simulations of ascending thoracic aortic aneurysms. Comput Fluids 165:96–115

Boffi D, Brezzi F, Fortin M et al (2013) Mixed Finite Element Methods and Applications, vol 44. Springer, Berlin

Brujan E (2010) Cavitation in non-Newtonian Fluids: With Biomedical and Bioengineering Applications. Springer, Berlin Heidelberg

Byrne G, Mut F, Cebral JR (2014) Quantifying the large-scale hemodynamics of intracranial aneurysms. Am J Neuroradiol 35(2):333–338

Chen R, Wu B, Cheng Z, Shiu W-S, Liu J, Liu L, Wang Y, Wang X, Cai X-C (2020) A parallel non-nested two-level domain decomposition method for simulating blood flows in cerebral artery of stroke patient. Int J Numer Methods Biomed Eng 36(11):3392

Coleman DM, Stanley JC (2015) Renal artery aneurysms. J Vasc Surg 62(3):779–785

Collard D, Brussel PM, Velde L, Wijntjens GW, Westerhof BE, Karemaker JM, Piek JJ, Reekers JA, Vogt L, Winter RJ et al (2020) Estimation of intraglomerular pressure using invasive renal arterial pressure and flow velocity measurements in humans. J Am Soc Nephrol 31(8):1905–1914

De Bruyne B, Manoharan G, Pijls NH, Verhamme K, Madaric J, Bartunek J, Vanderheyden M, Heyndrickx GR (2006) Assessment of renal artery stenosis severity by pressure gradient measurements. J Am Coll Cardiol 48(9):1851–1855

Deng W, Tsubota K-i (2022) Numerical simulation of the vascular structure dependence of blood flow in the kidney. Med. Eng. Phys. 104, 103809

Di Achille P, Tellides G, Figueroa C, Humphrey J (2014) A haemodynamic predictor of intraluminal thrombus formation in abdominal aortic aneurysms. Proc R Soc A Math Phys Eng Sci 470(2172):20140163

Di Gregorio S, Fedele M, Pontone G, Corno AF, Zunino P, Vergara C, Quarteroni A (2021) A computational model applied to myocardial perfusion in the human heart: from large coronaries to microvasculature. J Comput Phys 424:109836

Dobrek L (2021) An outline of renal artery stenosis pathophysiology-a narrative review. Life 11(3):208

Down LA, Papavassiliou DV, O'Rear EA (2013) Arterial deformation with renal artery aneurysm as a basis for secondary hypertension. Biorheology 50(1–2):17–31

Formaggia L, Nobile F, Quarteroni A, Veneziani A (1999) Multiscale modelling of the circulatory system: a preliminary analysis. Comput Vis Sci 2(2–3):75–83

Formaggia L, Gerbeau J-F, Nobile F, Quarteroni A (2001) On the coupling of 3D and 1D Navier-Stokes equations for flow problems in compliant vessels. Comput Methods Appl Mech Eng 191(6–7):561–582

Formaggia L, Lamponi D, Tuveri M, Veneziani A (2006) Numerical modeling of 1D arterial networks coupled with a lumped parameters description of the heart. Comput Methods Biomech Biomed Eng 9(5):273–288

Franca LP, Frey SL (1992) Stabilized finite element methods: II. The incompressible Navier-Stokes equations. Comput Methods Appl Mech Engrg. 99(2-3), 209–233

Grinberg L, Karniadakis GE (2008) Outflow boundary conditions for arterial networks with multiple outlets. Ann Biomed Eng 36:1496–1514

Grinberg L, Anor T, Madsen J, Yakhot A, Karniadakis G (2009) Large-scale simulation of the human arterial tree. Clin Exp Pharmacol Physiol 36(2):194–205

Klausner JQ, Lawrence PF, Harlander-Locke MP, Coleman DM, Stanley JC, Fujimura N, Itoga NK, Mell MW, Duncan AA, Oderich GS et al (2015) The contemporary management of renal artery aneurysms. J Vasc Surg 61(4):978–984

Klepaczko A, Szczypiński P, Strzelecki M, Stefańczyk L (2018) Simulation of phase contrast angiography for renal arterial models. Biomed Eng Online 17(1):41

Kong F, Kheyfets V, Finol E, Cai X-C (2018) An efficient parallel simulation of unsteady blood flows in patient-specific pulmonary artery. Int J Numer Methods Biomed Eng 34(4):2952

Lan H, Updegrove A, Wilson NM, Maher GD, Shadden SC, Marsden AL (2018) A re-engineered software interface and workflow for the open-source simvascular cardiovascular modeling package. J Biomech Eng 140(2):024501

Les AS, Shadden SC, Figueroa CA, Park JM, Tedesco MM, Herfkens RJ, Dalman RL, Taylor CA (2010) Quantification of hemodynamics in abdominal aortic aneurysms during rest and exercise using magnetic resonance imaging and computational fluid dynamics. Ann Biomed Eng 38(4):1288–1313

Lipowsky HH (2005) Microvascular rheology and hemodynamics. Microcirculation 12(1):5–15

Liu Y, Cai X-C (2021) A central-line coarse preconditioner for Stokes flows in artery-like domains. Numer Algorithms 87(1):137–160

Liu H, Lan L, Abrigo J, Ip HL, Soo Y, Zheng D, Wong KS, Wang D, Shi L, Leung TW et al (2021) Comparison of Newtonian and non-Newtonian fluid models in blood flow simulation in patients with intracranial arterial stenosis. Front Physiol 12:718540

Liu Y, Qi F, Cai X-C (2023) An aneurysm-specific preconditioning technique for the acceleration of Newton-Krylov method with application in the simulation of blood flows. Int J Numer Methods Biomed Eng 39(12):3771

Liu Y, Cai X-C (2023) Two-level additive Schwarz methods for three-dimensional unsteady Stokes flows in patient-specific arteries with parameterized one-dimensional central-line coarse preconditioner. J. Comput. Phys., 112290

Liu Y, Qi F, Cai X-C (2023) A one-dimensional coarse preconditioner for three-dimensional unsteady incompressible Navier-Stokes flows in patient-specific arteries. SIAM J. Sci. Comput., 1–23

Madhavan S, Kemmerling EMC (2018) The effect of inlet and outlet boundary conditions in image-based CFD modeling of aortic flow. Biomed Eng Online 17(1):66

Malek AM, Alper SL, Izumo S (1999) Hemodynamic shear stress and its role in atherosclerosis. JAMA 282(21):2035–2042

Mandaltsi A, Grytsan A, Odudu A, Kadziela J, Morris PD, Witkowski A, Ellam T, Kalra P, Marzo A (2018) Non-invasive stenotic renal artery haemodynamics by in silico medicine. Front Physiol 9:1106

Mariotti A, Antonuccio M, Morello M, Salvetti M, Celi S (2023) Numerical simulation of aortic coarctations of different grades of severity: flow features and importance of outlet boundary conditions. Comput Fluids 266:106043

Meng H, Tutino V, Xiang J, Siddiqui A (2014) High WSS or low WSS? Complex interactions of hemodynamics with intracranial aneurysm initiation, growth, and rupture: toward a unifying hypothesis. Am J Neuroradiol 35(7):1254–1262

Morales HG, Larrabide I, Geers AJ, Aguilar ML, Frangi AF (2013) Newtonian and non-Newtonian blood flow in coiled cerebral aneurysms. J Biomech 46(13):2158–2164

Morbiducci U, Ponzini R, Gallo D, Bignardi C, Rizzo G (2013) Inflow boundary conditions for image-based computational hemodynamics: impact of idealized versus measured velocity profiles in the human aorta. J Biomech 46(1):102–109

Moyle KR, Antiga L, Steinman DA (2006) Inlet conditions for image-based CFD models of the carotid bifurcation: is it reasonable to assume fully developed flow? J Biomech Eng 128(3):371–379

Perktold K, Resch M, Florian H (1991) Pulsatile non-Newtonian flow characteristics in a three-dimensional human carotid bifurcation model. J Biomech Eng 113(4):464–475

Pirola S, Cheng Z, Jarral O, O'Regan D, Pepper J, Athanasiou T, Xu X (2017) On the choice of outlet boundary conditions for patient-specific analysis of aortic flow using computational fluid dynamics. J Biomech 60:15–21

Qi F, Liu Y, Chen R, Hu P, Cai X-C (2025) Computational modeling of the kidney hemodynamics with a coupled unsteady Stokes-Darcy model. Int J Numer Methods Biomed Eng 41(11):70108

Qi F, Liu Y, Gong Y, Wang J-Y, Chen R, Hu P, Luo L, Cai X-C (2025) Towards a digital twin of the human kidney for diagnosis of renal diseases. In: 2025 International conference on metaverse computing, networking and applications (MetaCom), pp. 173–180 . IEEE

Qin S, Chen R, Wu B, Shiu W-S, Cai X-C (2021) Numerical simulation of blood flows in patient-specific abdominal aorta with primary organs. Biomech Model Mechanobiol 20(3):909–924

Quarteroni A, Veneziani A, Vergara C (2016) Geometric multiscale modeling of the cardiovascular system, between theory and practice. Comput Methods Appl Mech Eng 302:193–252

Reymond P, Merenda F, Perren F, Rufenacht D, Stergiopulos N (2009) Validation of a one-dimensional model of the systemic arterial tree. Am J Physiol Heart Circ Physiol 297(1):208–222

Saalfeld S, Voß S, Beuing O, Preim B, Berg P (2019) Flow-splitting-based computation of outlet boundary conditions for improved cerebrovascular simulation in multiple intracranial aneurysms. Int J Comput Assist Radiol Surg 14:1805–1813

Steele B (2007) Using one-dimensional finite element analysis to estimate differential pressure of renal artery stenoses. In: 2007 Computers in cardiology, pp 391–394 . IEEE

Steuer J, Bergqvist D, Björck M (2019) Surgical renovascular reconstruction for renal artery stenosis and aneurysm: long-term durability and survival. Eur J Vasc Endovasc Surg 57(4):562–568

Subramanian R, White CJ, Rosenfield K, Bashir R, Almagor Y, Meerkin D, Shalman E (2005) Renal fractional flow reserve: a hemodynamic evaluation of moderate renal artery stenoses. Catheter Cardiovasc Interv 64(4):480–486

Taylor TW, Yamaguchi T (1994) Three-dimensional simulation of blood flow in an abdominal aortic aneurysm-steady and unsteady flow cases. J Biomech Eng 116(1):89–97

Taylor CA, Hughes TJ, Zarins CK (1998) Finite element modeling of three-dimensional pulsatile flow in the abdominal aorta: relevance to atherosclerosis. Ann Biomed Eng 26:975–987

Valentin J (2002) Basic anatomical and physiological data for use in radiological protection: reference values: ICRP Publication 89. Ann ICRP 32(3–4):1–277

Vignon-Clementel IE, Figueroa CA, Jansen KE, Taylor CA (2006) Outflow boundary conditions for three-dimensional finite element modeling of blood flow and pressure in arteries. Comput Methods Appl Mech Eng 195(29–32):3776–3796

Weber BR, Dieter RS (2014) Renal artery stenosis: epidemiology and treatment. Int J Nephrol Renov Dis 169–181

Westerhof N, Lankhaar J-W, Westerhof BE (2009) The arterial windkessel. Med Biol Eng Comput 47(2):131–141

White CJ (2006) Catheter-based therapy for atherosclerotic renal artery stenosis. Circulation 113(11):1464–1473

Xiao N, Humphrey JD, Figueroa CA (2013) Multi-scale computational model of three-dimensional hemodynamics within a deformable full-body arterial network. J Comput Phys 244:22–40

Xiao N, Alastruey J, Alberto Figueroa C (2014) A systematic comparison between 1-D and 3-D hemodynamics in compliant arterial models. Int J Numer Methods Biomed Eng 30(2):204–231

Xu P, Liu X, Zhang H, Ghista D, Zhang D, Shi C, Huang W (2018) Assessment of boundary conditions for CFD simulation in human carotid artery. Biomech Model Mechanobiol 17(6):1581-1597

Yan Z, Yao Z, Guo W, Shang D, Chen R, Liu J, Cai X-C, Ge J (2022) Impact of pressure wire on fractional flow reserve and hemodynamics of the coronary arteries: a computational and clinical study. IEEE Trans Biomed Eng 70(5):1683–1691

Yim PJ, Cebral JR, Weaver A, Lutz RJ, Soto O, Vasbinder GBC, Ho VB, Choyke PL (2004) Estimation of the differential pressure at renal artery stenoses. Magn Reson Med 51(5):969–977

Zhang J, Harish K, Speranza G, Hartwell CA, Garg K, Jacobowitz GR, Sadek M, Maldonado T, Kim D, Rockman CB (2023) Natural history of renal artery aneurysms. J Vasc Surg 77(4):1199–1205

Zhou S, Xu L, Hao L, Xiao H, Yao Y, Qi L, Yao Y (2019) A review on low-dimensional physics-based models of systemic arteries: application to estimation of central aortic pressure. Biomed Eng Online 18(1):41